JACS
JOURNAL OF THE AMERICAN CHEMICAL SOCIETY
pubs.acs.org/JACS

Article

Interplay between β-Chitin Nanocrystal Supramolecular Architecture and Water Structuring: Insights from Three-Dimensional Atomic force Microscopy Measurements and Molecular Dynamics Simulations

Ayhan Yurtsever,*,¶ Kazuho Daicho,¶ Fabio Priante, Keisuke Miyazawa, Mohammad Shahidul Alam, Kazuki Miyata, Akinori Yabuki, Noriyuki Isobe, Tsuguyuki Saito, Adam S. Foster, and Takeshi Fukuma*

Cite This: J. Am. Chem. Soc. 2025, 147, 39134−39150

Read Online

ACCESS | Metrics & More | Article Recommendations | Supporting Information

ABSTRACT: Chitin, a highly abundant natural biopolymer, holds significant promise as a renewable resource; however, the structural organization and hydration properties of its β-crystalline form remain poorly understood, which limits our understanding of its fundamental characteristics. A thorough understanding of the three-dimensional (3D) supramolecular arrangement of chitin nanocrystals (NCs) in aqueous environments is crucial for realizing their full potential. Here, we employed atomic force microscopy (AFM) in combination with molecular dynamics simulations to elucidate the surface structure of individual β-chitin NCs at the single-fiber level under varying pH conditions. In situ AFM imaging reveals a highly ordered crystalline architecture with unprecedented molecular detail and demonstrates that water intercalation expands the lattice along the *b*-axis. 3D-AFM further revealed heterogeneous, pH-dependent hydration shells, forming an intricate 3D hydrogen bonding network around β-chitin NCs, thereby establishing substantial energetic barriers to direct interactions of external ions and molecules with the chitin surface and might lead to selective biomolecular interactions. Notably, α-chitin NCs exhibit stronger hydration forces than β-chitin NCs, reflecting distinct reactivities. Understanding the molecular assembly of β-chitin chains and their interactions with water across different pH values is critical for elucidating relevant biological processes and optimizing chitin decrystallization strategies. These findings advance our mechanistic understanding of the molecular assembly of water-intercalated β-chitin NCs, thereby enabling their efficient use in renewable products and supporting the rational design of functional and sustainable bionanomaterials.

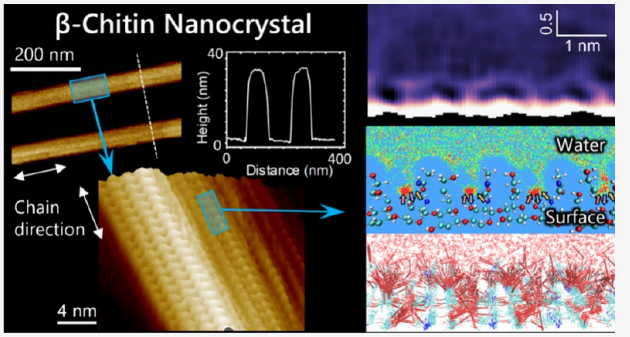

INTRODUCTION

Hierarchically structured nanomaterials derived from renewable resources have received considerable research attention in recent years, owing to their unique structural and chemical attributes, sustainability, lightweight, and natural abundance, offering environmentally friendly alternatives and advantages over their synthetic and inorganic counterparts.[1−3] Chitin, a renewable natural biomass resource, is highly abundant in marine crustacean shells, insect exoskeletons, and the cell walls of fungi, algae, and other living organisms, and it is essential in ensuring the structural integrity and mechanical strength of these organisms.[4] Chitin has exceptional mechanical properties, nontoxic nature, antibacterial capabilities, tunable surface architecture and chemistry, and renewable nature. This has promoted its significance in bioengineering,[5] particularly in drug delivery system development,[6] and it serves as a fundamental building block in the development of innovative functional nanomaterials.[1,7] An intriguing aspect of chitin nanocrystals (NCs) is their unique ability to self-assemble into hierarchical nanoarchitectures, displaying liquid nematic crystalline ordering in water and other aqueous solutions above a critical concentration.[8] This property enables their use in photonic devices.[9,10]

Over the past decade, these promising nanomaterials have been extensively studied for use in green electronics,[11] photoelectronic devices,[12] biosensing,[13] sensing devices,[14] self-healing hydrogels,[15] structural coloration,[3] water treatment,[16] catalysis,[17] bone-tissue engineering,[18] drug delivery,[19] shape-memory bionanocomposites,[20] and piezoelectric materials[21] and as reinforcing nanofillers for transparent polymers and composites.[22] The hierarchical organization of chitin at

Received: May 20, 2025
Revised: September 29, 2025
Accepted: September 30, 2025
Published: October 16, 2025

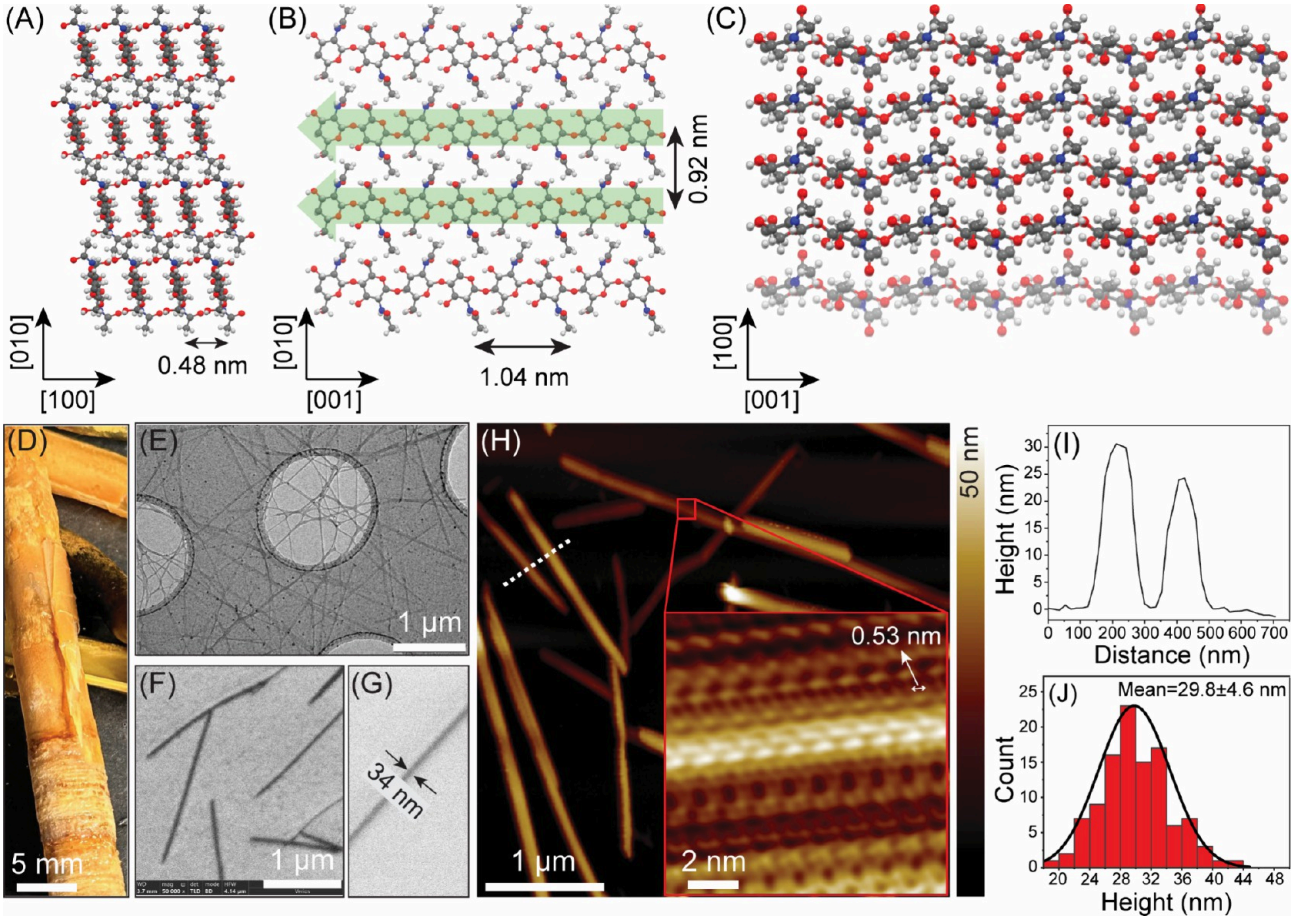

Figure 1. Molecular structure and morphology of β-chitin NC. (A–C) Ball-and-stick molecular models showing the arrangements of the chitin chain in β-chitin crystals from different perspectives, viewed orthogonal to the (A) *ab* plane with the chitin chain extending into the page, (B) *bc* plane, and (C) *ac* plane, emphasizing the parallel chain orientation. Carbon, oxygen, nitrogen, and hydrogen atoms are color-coded in gray, red, blue, and white, respectively. (D) Tubeworm sourced from Sagami Bay. (E) TEM micrograph of β-chitin NCs. (F and G) SEM images of β-chitin NCs dispersed on graphite. Magnification (F) 50,000× and (G) 100,000×. (H) An overview AFM image obtained in water, revealing well-dispersed, round-shaped nanostructures of β-chitin NCs spread onto a freshly prepared mica substrate. Inset: High-resolution AFM image of the surface structure at subnanometer resolution. (I) Representative line profile extracted along the dashed line in the cross-sectional direction, as indicated in (H). (J) Histogram showing the distribution of heights for individual β-chitin NCs (N = 100) obtained from different AFM images, revealing an average value of 29.8 ± 4.6 nm.

different length scales, along with its nanoscale structural and morphological details, significantly influences its functionality and applications and determines the properties of chitin-based nanomaterials.[23] Therefore, a thorough understanding of the three-dimensional (3D) supramolecular arrangement of the basic building blocks of chitin NCs in aqueous environments is essential for realizing the full potential of these nanomaterials and expanding their applications in the development of advanced, smart nanostructured materials.[24]

Chitin exists in nature in two major crystalline-allomorph forms, the α- and β-forms, depending on its source.[4] The differences between these crystal allomorphs arise from the different packing organizations and orientations of adjacent chitin chains in alternating sheets.[25,26] In α-chitin, the molecular chains are structured in an antiparallel arrangement within the unit cell, forming an orthorhombic two-chain unit lattice,[27] whereas, in β-chitin, they are organized in a parallel manner,[28,29] with a monoclinic one-chain unit cell adopting P21 symmetry (Figure 1A–C). The antiparallel packing of the α-chitin chains results in a higher degree of hydrogen bonding and higher resistance to thermal degradation[30] compared to β-chitin. Notably, the hydrogen bonding patterns differ markedly between α- and β-chitin, which significantly affects their intermolecular interactions and solvation behavior. In β-chitin, a lower density of intersheet hydrogen bonds results in weaker intersheet interactions compared to the extensive hydrogen bonding network in α-chitin, thereby allowing water and other small molecules, such as alcohols, amines, and glucose, to intercalate between the sheets.[31] These structural features provide β-chitin with increased flexibility and accessibility while exposing surface functional groups that enhance its chemical reactivity relative to α-chitin. This unique ability of β-chitin to accommodate water within its crystal lattice, along with the resulting structural modifications, imparts distinct physicochemical properties that critically influence its biological functions, environmental adaptability, and potential material applications.

Chitin is typically sourced from the carapace of crustaceans, insects, crabs, and shrimps as well as the cell walls of fungi.[7] The less prevalent β-type chitin is mainly found in tubeworms, squid pens, and marine diatoms.[4,28] To fully exploit the potential of these abundant and sustainable nanomaterials, their diverse polymorphic forms must be thoroughly characterized, particularly with submolecular resolution at the

https://doi.org/10.1021/jacs.5c08484
J. Am. Chem. Soc. 2025, 147, 39134–39150

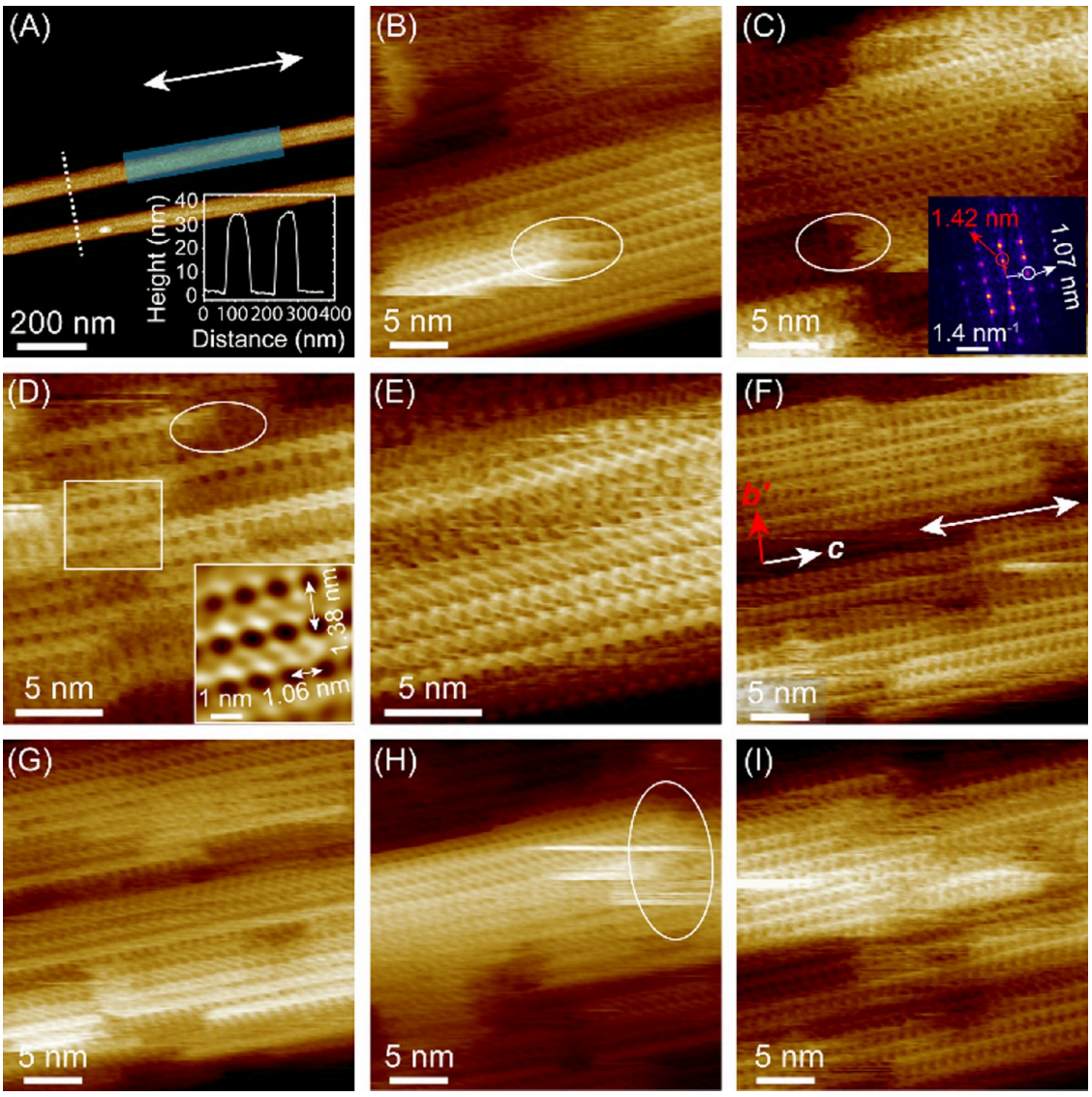

Figure 2. Variation in molecular arrangements on chitin NC surfaces. (A) AFM topography image showing two individual β-chitin NCs on mica, acquired in water. Inset: Height profile across the chitin NCs, revealing a height of 32 nm. (B–I) High-resolution AFM images recorded along the fiber axis (across the shaded region in (A)), each covering an area of 20–30 nm × 20–30 nm, revealing the structural variations across the crystal surface. The inset image in (C) displays the FFT pattern derived from the central region of the image, revealing lattice parameters of 1.42 nm along the lateral (b'-axis) and 1.07 nm along the c-axis. This suggests that AFM resolves the (1–20) crystalline plane of the parallelogram-shaped NCs. The inset image in (D) shows the filtered AFM image of the framed region, demonstrating a well-ordered chain arrangement. Ellipses highlight regions with fluctuating disordered domains on the surface, indicating the boundary between vertically stacked chitin sheets.

single-fiber level in their aqueous environments. While our previous study[32] revealed the submolecular structural arrangements and assembly of the α-chitin polymorph from shrimp, as well as the associated 3D local molecular structures of water at its surfaces, a critical gap remains in our understanding of β-chitin NCs. In particular, the molecular-level details of water intercalation and 3D hydration structures at the β-chitin/water interface have not been experimentally resolved, despite β-chitin's fundamentally different parallel chain organization, distinctive hydrogen bonding pattern, and capacity to accommodate water and small polar molecules between its molecular sheets, resulting in the formation of intercalation complexes.[33−35] These properties make β-chitin a compelling model for studying water structuring at biopolymer interfaces. In this study, we address this knowledge gap by combining high-resolution atomic force microscopy (AFM) with molecular dynamics (MD) simulations to elucidate the supramolecular organization and interfacial hydration architecture of water-intercalated β-chitin. Building upon this structural and interfacial analysis, we next investigate the influence of pH—given that it is a critical factor governing water structuring at solid–liquid interfaces, pH-dependent investigations are essential to elucidate its impact on the molecular organization of chitin NCs and the 3D hydration architecture surrounding them—an aspect that has been largely overlooked at the molecular scale yet is crucial to their biological function under diverse pH conditions.

An understanding of the differences in the interfacial hydration and solvation structures between α- and β-chitin NCs under different pH conditions may help to elucidate the origins of their distinct reactivities. This, in turn, not only improves our knowledge of chitin binding selectivity, such as

https://doi.org/10.1021/jacs.5c08484
J. Am. Chem. Soc. 2025, 147, 39134−39150

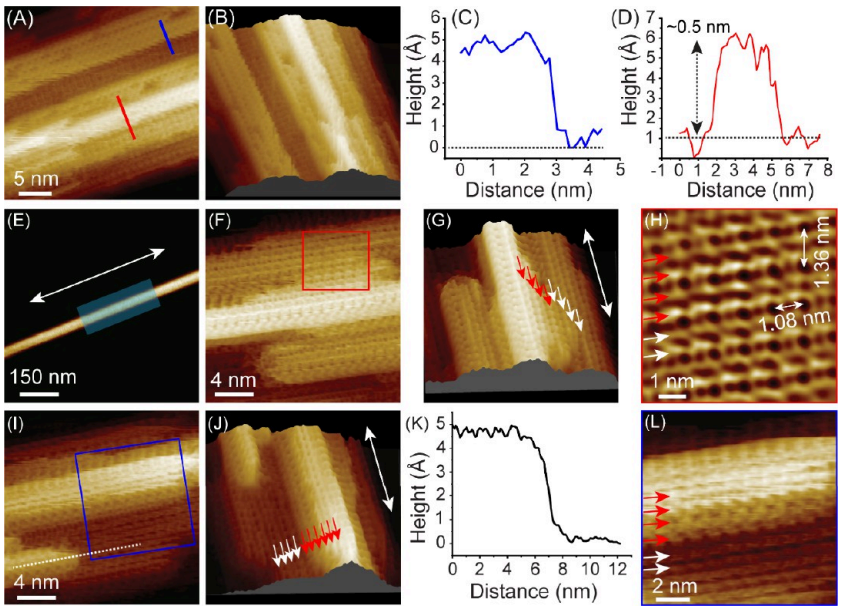

Figure 3. Molecular details at the boundary between different chitin structural domains. (A) High-resolution AFM topography image of a part of the chitin NC surface. (B) 3D view. (C, D) Height profiles along the blue and red lines in (A), showing layered molecular arrangements with layer heights of 0.47−0.50 nm, respectively, corresponding to a single layer of the chitin sheet. (E) AFM image of an individual chitin fiber. (F) High-resolution AFM topography image of part of the chitin NC surface. (G) 3D view. (H) AFM image of the framed region in (F), revealing the structural details of the boundary region. (I) High-resolution AFM topography image of a part of the chitin NC surface. (J) 3D view. (K) Height profile along the white dashed line in (I), showing layered molecular arrangements with layer heights of 0.47−0.50 nm, respectively, corresponding to a single layer of the chitin sheet. (L) AFM image of the framed region in (I), revealing the structural details of the boundary region.

polymorph-selective peptide-chitin interactions,[36] but also provides a foundation for the rational design of chitin-based nanomaterials with tailored hydration properties, reactivity profiles, and biological function.

The 3D structuring of water around chitin NCs strongly influences the properties of chitin-based nanomaterials and is crucial for understanding various aspects of chitin NCs. These include their self-assembly into chiral nematic structures, interactions with other nanomaterials, reinforcement efficiency in nanocomposites, and interfacial mechanical and rheological properties. The molecular organization of water surrounding chitin NCs further contributes to an understanding of their molecular recognition properties, such as interactions with peptides,[36] and biochemical processes, including the chemical and enzymatic hydrolysis of chitin. Water structuring is a key factor governing the rate and mechanism of these chemical reactions, significantly affecting hydrolysis kinetics and product release and contributing to the high energy demands involved in the commercialization and processing of chitin-based nanomaterials. Additionally, this understanding sheds light on the formation and dynamics of biomolecular assemblies and intercalation complexes on chitin NC surfaces.[37] Consequently, investigating and tailoring water−chitin interactions provide molecular-level insights into essential biological processes and aid the development of novel, functional, and sustainable bionanomaterials through a bottom-up design approach.

In this study, we used AFM combined with MD simulations to investigate the supramolecular assembly of chitin chains within crystalline β-chitin intercalated with water. High-resolution AFM imaging under varying pH conditions revealed unprecedented molecular details of β-chitin NC surface organization. 3D-AFM measurements, complemented by MD simulations of water density distributions, elucidated the local molecular structure and organization of hydration layers surrounding β-chitin NCs. The results demonstrate strong chitin−water interactions, leading to pronounced and well-organized interfacial water structuring, governed by the unique architecture and surface chemistry of β-chitin, as well as the accessibility of its functional groups for hydrogen bonding. These interactions result in the inhomogeneous encapsulation of chitin surfaces by a 3D hydrogen-bonding network, imposing significant energetic barriers to the direct association of external ions and molecules. Comparative analysis revealed that α-chitin NCs exhibit stronger hydration forces than β-chitin, suggesting a higher energetic penalty for molecular interactions at the α-chitin interface, which may account for their differing reactivity. These insights into the molecular-level structural characteristics and hydration behavior of chitin NCs enhance our understanding of crystallosolvate and inclusion complex formation within β-chitin[34,38,39] and will facilitate the rational design and functionalization of chitin-based functional nanomaterials for applications in materials science, biotechnology, and pharmaceuticals.

RESULTS AND DISCUSSION

Structural and Morphological Characteristics of Water-Intercalated β-Chitin NCs. β-chitin NCs were prepared via hydrochloric acid hydrolysis followed by mechanical treatment and ultrasonication, and their morphology and size distribution were assessed using transmission electron microscopy (TEM), scanning electron microscopy (SEM), and frequency-modulation AFM (FM-AFM) (Figures 1D-H). A diluted aqueous suspension of purified β-chitin NCs obtained from *Lamellibrachia columna* (Figure 1D) was deposited onto a freshly cleaved mica surface and observed by using FM-AFM in water. The morphological characteristics of the tubeworm-derived β-chitin NCs are presented in Figure

https://doi.org/10.1021/jacs.5c08484
J. Am. Chem. Soc. 2025, 147, 39134−39150

1H, which shows an AFM image of the β-chitin NCs spread across the mica surface. The resulting AFM observations of β-chitin NCs showed individual and well-dispersed straight fibers with lengths ranging from 500 nm to several micrometers. The histogram analysis for the sizes of chitin NCs derived from different samples reveals a height-distribution range of 15−45 nm with an average value of 29.8 ± 4.6 nm (based on measurements of 100 individual chitin NCs with well-defined edges or boundaries) (Figure 1I,J). The dimensions of β-chitin NCs are consistent with those reported in previous studies for acid-hydrolyzed β-chitin NCs derived from tubeworms and are also confirmed by our TEM (Figure 1E) and SEM measurements (F, G). At intermediate resolution, the chitin fibers appeared to have a smooth and round surface with a uniform height (Figures 1H and S1). However, closer examination at the molecular level revealed intricate molecular arrangements (Figure 1H, inset), which are discussed in detail below.

Molecular Arrangements of Chitin Chains and Their Crystalline Ordering at the Surfaces of β-chitin NCs. The molecular arrangements of elementary chitin chains and their crystalline order at the surfaces of individual chitin NCs are shown in Figures 2 and S2. A series of localized high-resolution AFM images, each covering an area of 20−30 nm × 20−30 nm above a single chitin fiber (highlighted area in Figure 2A), was acquired along and across the chitin-fiber axis to resolve the crystalline-chain arrangements and their molecular assemblage in the 3D crystalline structure as well as identify potential surface defects or imperfections. The AFM observations at molecular resolution across the fiber surface confirmed the existence of a well-organized crystalline arrangement that extends across most of the crystal surface without considerable structural defects, i.e., disordered domains (Figure 2B−I). However, the surface areas marked with ellipses exhibit discrete, layered molecular stacking with crystalline ordering (Figure 2B−D,H,I). This structural feature likely results from the peeling of chitin chains in localized domains during mechanical treatment or from the delamination of chitin layers induced by mechanical forces generated during ultrasonic processing.[12,40]

The surfaces of individual β-chitin NCs generally exhibit high surface crystallinity and significant chain ordering over large domains, but individual chains do not extend continuously along the crystal axis. Instead, chains exhibit breaks at certain points along their length, resulting in discrete layered structural arrangements in some domains. These molecular arrangements lead to a structure resembling partially bitten corncobs or a brickwork pattern (Figures 2 and S2). A representative molecular-resolution AFM image of a portion of the chitin-NC surface, showing a layered structural arrangement along the length of the fiber, is demonstrated in Figure 3 (see also Figure S3). The layered molecular arrangement of chitin sheets within the fiber is clearly visualized in Figure 3A,B, where the sheets extend along the fiber axis and are separated by heights of 0.47−0.50 nm (Figure 3C,D), consistent with the spacing of a single chitin layer assembled along the a-axis of the crystals. The high-resolution molecular details of the lateral boundary between different chitin-chain fragments in layered arrangements, as recorded above the chitin fiber in Figure 3E and highlighted by red and blue squares in Figure 3F−G,I−K, are shown in Figure 3H,L, respectively. The seamless alignment of the lattice with the registry of the underlying chitin layer demonstrates the continuity at the lateral boundaries among different layered fragments of the chitin NCs (Figure 3H,L). The apparent continuity of the molecular arrangements at the boundary suggests that these different structural components are not merely external aggregates; instead, they constitute an integral part of the chitin fiber.

Discrete or layered stacking of chitin chains disrupts the regularity of lateral packing, making it challenging to determine the molecular periodicity in the lateral direction. We determined the molecular spacing along the lateral direction (i.e., the b'-axis) in the surface region characterized by one-phase molecular ordering and relatively flat geometry, as shown in Figures 2C,D, 3D, 4, and S4, and S5. An average

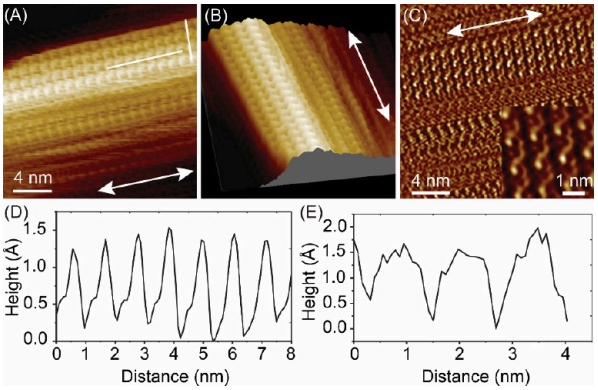

Figure 4. Representative AFM images of β-chitin NC in water, showing the uniform molecular organization of the chains, characterized by relatively small lattice spacing. (A) AFM image of an individual β-chitin NC, revealing the crystalline arrangement of the surface-chitin chains. (B) 3D rendering of the AFM topography image in (A), providing a detailed visualization of the chitin NC surface at the molecular level. (C) Corresponding AFM dissipation image of the surface in A. (D, E) Height profiles along the white lines in (A) illustrate the periodicity in both the longitudinal and transverse directions, respectively, consistent with imaging of the (1−20) crystalline plane.

periodicity of 1.07 ± 0.1 nm was measured along the chitin chain axis, which is in excellent agreement with the crystallographic repeat of the chitobiose unit (1.04 nm), while the lateral chain-to-chain spacing was determined to be 1.40 ± 0.1 nm (Figure S6), closely matching the MD-simulated value of 1.38 nm above the (1−20) crystalline plane (Figures S7 and S8). It is worth noting that the bulk lattice parameter along the b-axis is 1.12 nm for the dihydrate form chitin NCs; however, when the cross-sectional shape of the crystal is taken into account, the effective periodicity of molecular features along the lateral direction—denoted as b'—is calculated to be 1.38 nm. While these values agree with those determined by the MD simulations, smaller spacings between molecular features along the lateral direction are occasionally observed on some chitin NC surfaces (Figures 4, S9, and S10), suggesting the presence of a different chitin NC cross-sectional shape and/or varying structural arrangements of chitin NCs.

The molecularly resolved AFM image shown in Figure 4A and its corresponding 3D rendering (Figure 4B) exemplify chitin fibers with relatively smaller periodicity along the b'-axis, displaying a uniform crystalline surface free of surface imperfections or defects. The corresponding AFM dissipation image is depicted in Figure 4C. The 2D-FFT pattern is indicated as an inset image, displaying well-aligned molecular chains with detailed substructures in both the lateral and

https://doi.org/10.1021/jacs.5c08484
J. Am. Chem. Soc. 2025, 147, 39134−39150

perpendicular directions. Height profiles taken along and perpendicular to the chitin chain axis demonstrate a periodicity of 1.08 nm along the chains and 1.22 nm in the lateral direction perpendicular to the molecular axis (Figure 4D,E).

The chains in both α- and β-chitin NCs are organized such that they form sheets that are held together by intrasheet hydrogen bonds. Several intersheet hydrogen bonds exist along the b parameter in α-chitin; however, they are absent from the β-chitin structure (where hydrogen bonding occurs exclusively within sheets, i.e., mainly on the ac plane). The β-chitin structure is more susceptible to crystalline swelling than α-chitin when exposed to water, alcohols, and amines.[39] Owing to the lack of intersheet hydrogen bonds between hydrophobically stacked molecular sheets, β-chitin NCs can accommodate various small polar molecules within their crystal lattices as intercalates, leading to the formation of several crystallosolvates or crystalline complexes.[33−35] The swelling of β-chitin NCs results in lateral expansion of the b parameters in the unit cell. The X-ray diffraction (XRD) measurements were used to determine the crystallinity of the prepared nanocrystals and study their structural properties in wet and dry states. Figure 5 shows the XRD profiles of β-chitin

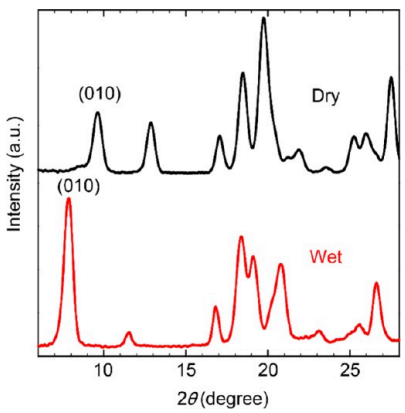

Figure 5. Comparison of XRD Patterns for β-chitin NCs in dry and wet states. Equatorial XRD profile of anhydrous β-chitin (top) and hydrated β-chitin (bottom). A noticeable shift of the 010 peak toward a lower angle is observed, indicating an increase in the interplanar spacing (d-value).

in the dry and wet states. A shift of the 010 diffraction to a lower angle, from 9.2° in the dry state to 7.7° in the wet state, is observed. This indicates an expansion of the bulk lattice parameter of anhydrous β-chitin from 0.92 to 1.12 nm along the b-axis, which is in good agreement with previous averaging methods, such as XRD and NMR measurements.[29,33,35] As noted above, molecular-scale AFM images of β-chitin NCs revealed variations in the intermolecular periodicity of the molecular features along the b'-axis of the crystal structure. The MD simulation of the water-intercalated chitin NC model structure reveals a periodicity of 1.38 nm between molecular features along the b'-axis on the (1−20) crystal plane (Figures 8A, S7, and S8). This is consistent with our experimental results (Figures 2C,D, 3D, and S4−S6) and suggests lattice expansion due to water intercalation, as previously observed in diffraction studies on β-chitin dihydrate.[41] As the chitin nanocrystals are fully hydrated in water, complete intercalation is expected, ruling out intercalation heterogeneity—such as partial or nonintercalated domains—as the source of the observed variability in molecular periodicity along the b'-axis. However, the potential structural differences between individual chitin NCs may result in different periodicities along the b'-axis, as evidenced by some TEM cross-sectional measurements.[42] To verify this, we performed MD simulations of various molecular structures with differing angles of parallelogram-shaped chitin nanostructures. The slight angle changes between the (1−20) and (010) crystalline planes resulted in variations in periodicity that accurately reproduced the experimentally observed differences in intermolecular periodicities along the b'-axis (Figure S8).

3D-AFM Characterization of Local Hydration Structures around Crystalline β-Chitin. We extended our investigation by using 3D-AFM measurements to generate 3D force maps, enabling a detailed assessment of water−chitin interactions and the resulting water structure around the crystalline facets of β-chitin NCs. The 3D-AFM method with small-amplitude oscillation[43] has proven its ability to determine intricate 3D local hydration/solvation structures at various interfaces with unprecedented structural detail, including crystalline solid surfaces,[44−53] solid−electrolyte interfaces,[54] soft lipid head groups,[55] and structural biopolymers.[56] We previously investigated the behavior of water molecules in close proximity to a multifaceted crystalline α-chitin NC, highlighting the highly structured nature of water molecules at different crystalline interfaces.[32] However, no studies have investigated the behavior of water in the vicinity of β-chitin NCs, where the molecular chain arrangements and hydrogen-bonding patterns differ significantly from those of α-chitin; in β-chitin NCs, intermolecular bonds occur solely between chitin chains in the ac plane of the crystal.[7]

A representative 3D Δf map of the β-chitin−water interface is shown in Figure 6, revealing the spatial local structural arrangement of water molecules around individual β-chitin NCs in the 3D interfacial space. Large-amplitude 2D FM-AFM measurements were initially performed to investigate the molecular assembly at the interface (Figure 6A), providing a clear visualization of individual chitin chains (see the inset image). Subsequently, 3D-AFM Δf volume maps were generated using smaller oscillation amplitudes (0.1−0.2 nm) over a localized surface region (15 nm × 15 nm × 3 nm, 128 × 128 × 256 pixels) (Figure 6B,C). The resulting 3D Δf map reveals the presence of subnanometer molecular features indicative of the local hydration structure near the interface above the chitin NC (Figure 6C). These laterally and vertically well-organized water structures were observed to encapsulate the entire crystal surface, extending approximately 6−7 Å from the nearest surface to the bulk water, as determined from the 3D Δf maps obtained from different samples.

Horizontal slices were extracted from the 3D volume maps to gain a more detailed understanding of the molecular structures of the interfacial water, providing a 2D XY-plane view of the interface at different z-heights ranging from the closest surface to the bulk water. The evaluation of in-plane molecular organization of water within the hydration layers is demonstrated by 2D Δf slices acquired at z-heights of 0.3−0.7 nm, as shown in Figure 6D−I. A nonuniform arrangement of water molecules within the interfacial water layer, even within small local areas, is apparent in the 2D in-plane Δf maps, with periodic molecular features forming distinct 2D hydration patterns. In particular, in the upper region of the 2D XY Δf maps (highlighted with yellow rectangle), the hydration pattern undergoes a structural transition from dimer or dot-like features at z-distances closer to the surface (in the z-range

https://doi.org/10.1021/jacs.5c08484
J. Am. Chem. Soc. 2025, 147, 39134−39150

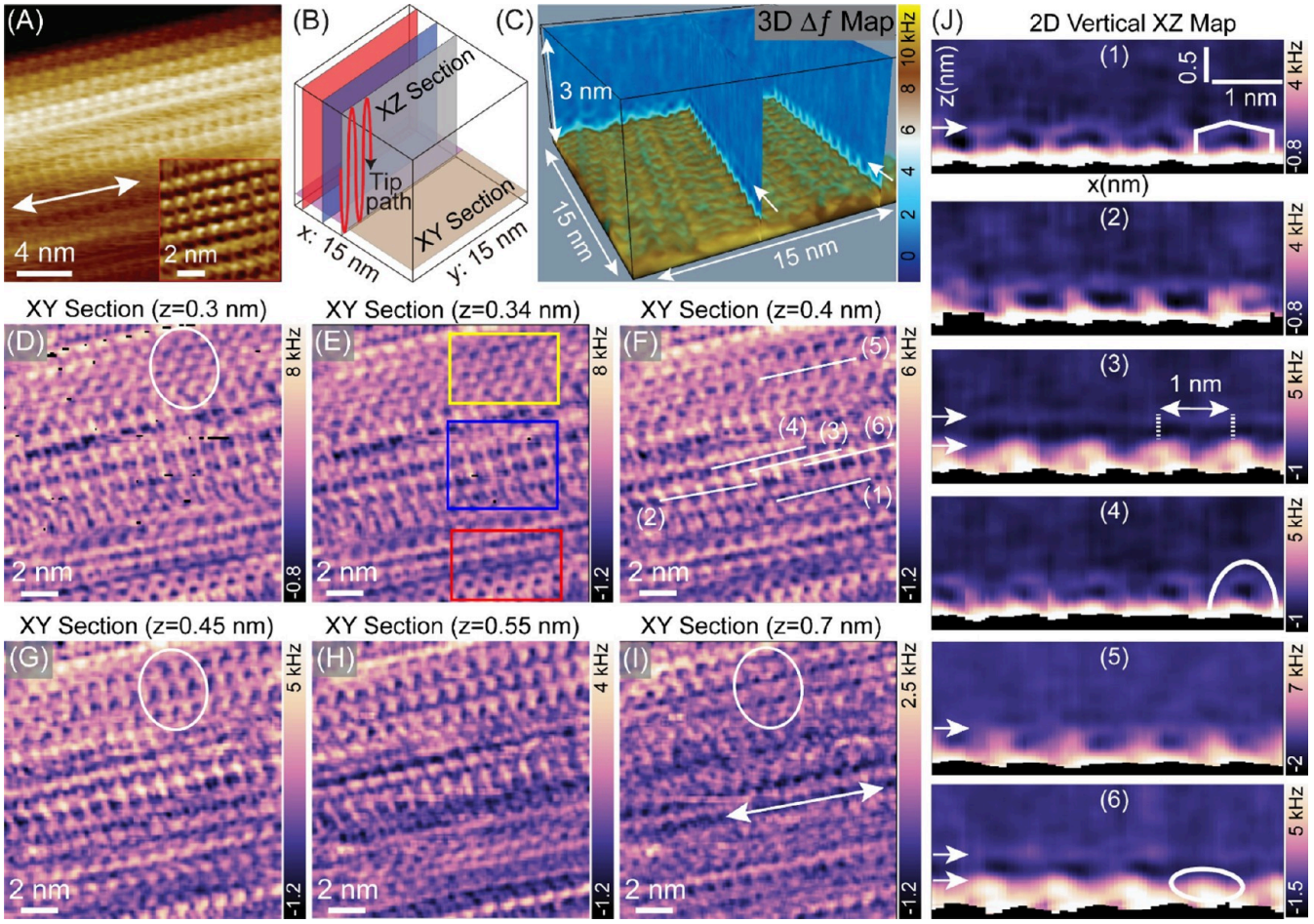

Figure 6. Representative 3D-AFM images of the β-chitin−water interface. (A) 2D FM-AFM image of the β-chitin−water interface, acquired with a large-amplitude cantilever oscillation (~0.5 nm). Inset: FFT filtered image of the top region of the surface. (B) Schematic showing the trajectory of the tip in the 3D-AFM technique in 3D interfacial space, along with a description of the 2D-*xz* and *xy* slices in the 3D volume map. (C) 3D-AFM Δf map of the β-chitin−water interface, acquired over the upper part of the surface shown in (A), exhibiting the variations of the Δf of the oscillating cantilever in the 3D interfacial space. The white arrows indicate the ordered layer of water molecules at the interface. (D−I) In-plane 2D-*xy* Δf maps of the chitin−water interface, extracted from the 3D volume map at the vertical *z*-positions indicated on each image. (J) Vertical 2D-*xz* Δf maps of the chitin−water interface along the dashed lines marked in (F). The dark regions at the bottom of the 2D *XZ* slices show no data points (J). The 3D map was constructed from 16384 (128 × 128 pixels) data sets obtained above the (1−20) crystalline plane.

of 0.3−0.35 nm) to extended hydration features oriented perpendicular to the chitin molecular axis at *z*-distances of 0.4−0.55 nm, bridging two molecular chains at the interface (these structural changes are highlighted by white ellipses). In the central region of the 2D *XY* sections (blue rectangle), identical hydration contrast patterns with similar orientations are observed at *z*-distances of 0.3−0.45 nm. In the lower part of the 2D *XY* sections (red rectangle), a circular hydration pattern emerges at *z*-distances closer to the substrate, evolving into a straight line aligned along the fiber axis and eventually disappearing at z-distances larger than 0.7 nm.

The vertical organization of the interfacial water structures can be assessed by taking vertical slices through the z-plane along the X or Y directions in the 3D maps. The vertical 2D XZ slices along the molecular chain axis at different lateral positions (marked with dashed lines in Figure 6F) reveal the presence of well-localized hydration structures with distinct molecular arrangements and varying lateral XYZ spatial dependence (Figure 6J). The molecular features observed within the hydration layers across local domains at the interface differ in size, structure, and extension, suggesting variations in the nature of interactions between water molecules and surface-chemical moieties. These findings indicate that proximity to the crystalline surface introduces significant heterogeneity in the distribution, organization, and structures of water at the molecular scale (Figure 6J; Figures S11−S15). We next investigated the behavior of water molecules above the β-chitin NC with a layered molecular arrangement to elucidate how water is structured over different structural domains and boundary regions. The horizontal, in-plane (Figures 7A−C), and vertical (Figure 7D−K) Δf maps across the different structural layers of chitin NC indicate that the structured water forms a continuous layer that encapsulates the underlying molecular structure of chitin, bridging the domain boundaries between different layers (see also Figure S11). We also observed the emergence of two distinct hydration structures at the interface: one with relatively thick layers (Figure 7D−F) and the other with relatively thin layers (Figure 7G−I). This distinction is further emphasized by 1D force−distance curves, which show a larger repulsive force above the thicker hydration layer (Figure 7M) compared to the thinner one (Figure 7L). These observations suggest that the interaction between water molecules and the β-chitin surface is nonuniform and that the molecular structure and

https://doi.org/10.1021/jacs.5c08484
J. Am. Chem. Soc. 2025, 147, 39134−39150

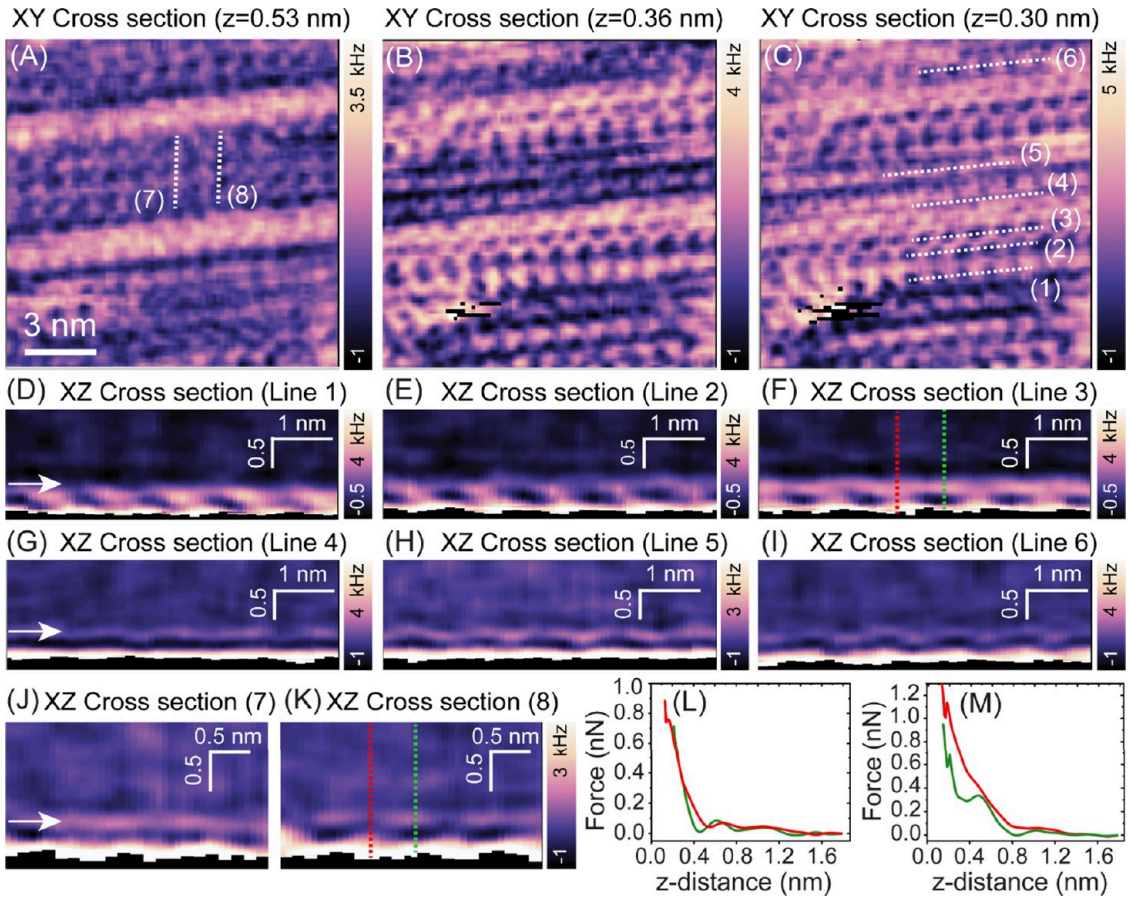

Figure 7. Representative 3D map of the β-chitin−water interface with layered molecular arrangement. (A−C) 2D *XY* cross-sectional images of the chitin−water interface, extracted from the 3D volume map at the vertical z-positions: (A) z = 0.53 nm, (B) z = 0.36 nm, and (C) z = 0.3 nm, showing the in-plane molecular organization of water near the chitin surface. (D−I) Vertical 2D-*xz* Δf maps of the chitin−water interface along the dashed lines marked in (C). (J, K) Vertical 2D-*xz* Δf maps of the chitin−water interface along the direction perpendicular to the fiber axis (marked in panel A). (L, M) Individual force−distance curves along the dashed lines shown in (K, F), respectively. Force mapping area has dimensions of 14 nm × 14 nm and is divided into grids of 179 × 179 pixels, obtained above the (1−20) crystalline plane. The dark region at the bottom of the 2D vertical slices indicates the absence of data points.

thickness of the hydration layer can vary depending on specific surface features and/or domains in the *XY* surface plane. The observed heterogeneity in hydration structures and the associated forces suggest a complex interplay between the β-chitin surface and surrounding water molecules. Such heterogeneity may arise from variations in local charge distribution, molecular arrangements, and the accessibility of functional groups that modulate water−surface interactions. Although the chemical treatment conditions used in this study are relatively mild and are not expected to cause significant deacetylation or oxidation, localized morphological changes—particularly those introduced during sonication—may also contribute to surface heterogeneity. These variations could, in turn, influence the extent and spatial distribution of water structuring near the chitin surface (Figures S11−S13). At the boundary, as indicated by the ellipses in Figure 2, a fluctuating hydration structure forming a continuous, dynamic layer near the crystal surface was observed (Figures S12 and S13). The force−distance curves do not display a characteristic oscillatory force profile; instead, they show a continuous, purely repulsive interaction that increases monotonically as the surface is approached. This behavior is likely due to (i) the presence of unstable hydration structures and (ii) the fluctuation of surface functional groups, along with their associated hydration layers. The heterogeneity observed in the hydration structures was further validated by FT-IR spectroscopy measurements, which resolved multiple peaks within the OD stretching region (Figure S16). These peaks indicate the presence of diverse hydrogen bonding configurations, thereby reflecting the underlying structural heterogeneity.

MD Simulation of Water Density Distribution Near β-chitin NCs. We next performed MD simulations to gain a molecular-level understanding of the observed 3D water interface structure in the vicinity of the crystalline β-chitin NCs. A parallelogram-shaped molecular structure of β-chitin NC was constructed through an eight-layer molecular sheet arrangement of 198 chitin chains (Figure 8A). The cross-sectional shape of β-chitin NCs derived from *L. columna* was previously determined by high-resolution TEM investigations.[42] A molecular-packing model for the β-chitin NCs with a parallelogram shape was established[42] by employing the structural model proposed by Nishiyama et al.,[28] based on XRD measurements. We adopted this cross-sectional shape with an identical molecular-packing structure to capture the 3D spatial molecular arrangements and density distribution of interfacial water molecules around the β-chitin crystal (Figures S17−S19). The simulated 3D water density maps near all exposed crystalline planes of the parallelogram-shaped chitin

https://doi.org/10.1021/jacs.5c08484
J. Am. Chem. Soc. 2025, 147, 39134−39150

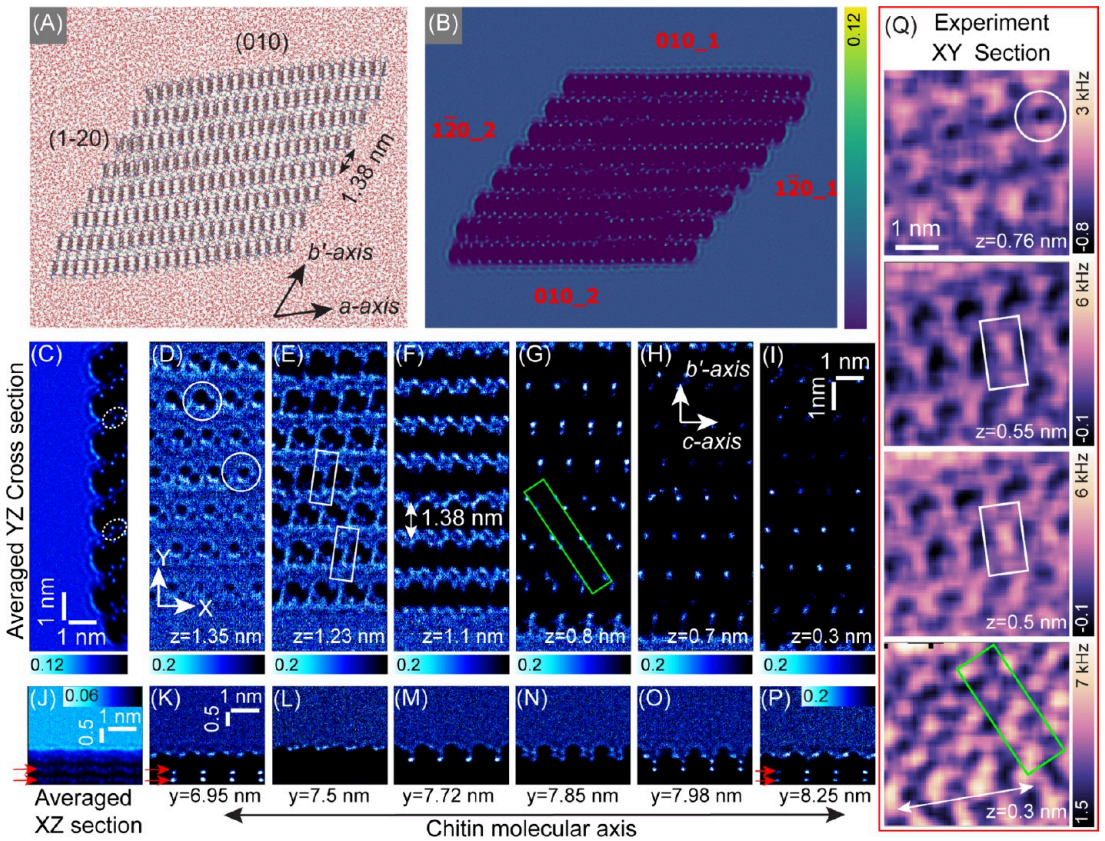

Figure 8. Simulated water density distribution around a parallelogram-shaped β-chitin NC surface. (A) Molecular dynamics snapshot showing a 198-chain fibril model of a parallelogram-shaped β-chitin NC solvated with water. The NC consists of eight layers of chitin sheets, exposing several crystallographic planes. The simulation box is viewed along the *c* crystallographic axis. (B) 3D map of water-oxygen density around a parallelogram-shaped β-chitin NC with exposed crystallographic planes (labeled). (C) Averaged vertical 2D density profile of water-oxygen atoms above the (1−20) crystallographic plane, taken through the *zy* plane along the direction perpendicular to the chain axis, i.e., *b*′-axis. (D−I) 2D horizontal water-density slices extracted from the 3D map at different vertical *z*-heights. (J) Averaged vertical 2D density profile above the (1−20) crystalline plane, sectioned through the zx plane along the direction parallel to the chain axis. (K−P) Vertical 2D water density maps along the chain direction for different lateral positions. (Q) Experimentally obtained 2D horizontal maps of the chitin−water interface at different *z*-heights. The red arrows in panels J, K, and P indicate the intercalated water molecules.

NC model are shown in Figure 8B. The simulated density contours reveal that the water molecules are highly structured by the β-chitin NC surface. As the water molecules approach the crystal surface and interact with its functional groups, they transform into a localized structure, occupying specific positions near the surface and resulting in a complex 3D arrangement and distribution of water at the interface. The interactions with specific surface functional groups, characterized by distinct hydrophobic and hydrophilic properties, together with the molecular topology of the crystal surface, constrain water molecules to defined regions, forming structures with specific shapes. This confinement leads to variations in the water density across the 3D interfacial space, where some areas exhibit either increased or decreased density. This highly organized structure extends up to 0.6−0.7 nm from the crystal surface, in agreement with experimental results. The spatial molecular arrangement and packing of the chitin chains in β-chitin NCs have different effects on the water density distribution across different crystalline planes. Differences in molecular structures, roughness, molecular-packing, intra- and interlayer hydrogen bonding networks, and heterogeneous arrangements of surface-chemical moieties contribute to the formation of distinct water density distributions and structures above the different crystalline planes labeled (010) and (1−20). A comparison of simulated oxygen density maps above the (010) crystalline plane is shown in Figure S20. Water molecules can intercalate through chitin layers above the (1−20) crystalline plane, resulting in lattice parameter expansion along the *b*′-axis. In contrast, intercalation above the (010) crystallographic plane is impeded. Figure 8C shows the simulated averaged 2D vertical water-oxygen density distribution along the direction perpendicular to the chitin chain axis, i.e., averaged over the cross section of the (1−20) crystallographic plane. This 2D vertical density contour reveals an arch-shaped hydration structure characterized by a wavy profile, indicating a large variation of the water density distribution extending approximately 15 Å into the interfacial region, including the intercalated water (highlighted by white ellipses). The variation of the water density distribution at the (1−20) interface is larger than that of the structured water density variations at the (010) crystal plane, which has a relatively flat density profile (see Figure S20). This difference occurs because the (1−20) plane has a rugged and sawtooth surface structure with deep and wide grooves that facilitate the intercalation of water molecules. These result in the formation of a stable complex by participation in multiple hydrogen bonds with the exposed hydrophilic chemical moieties at the interfaces and in the crystalline interior.

https://doi.org/10.1021/jacs.5c08484
J. Am. Chem. Soc. 2025, 147, 39134−39150

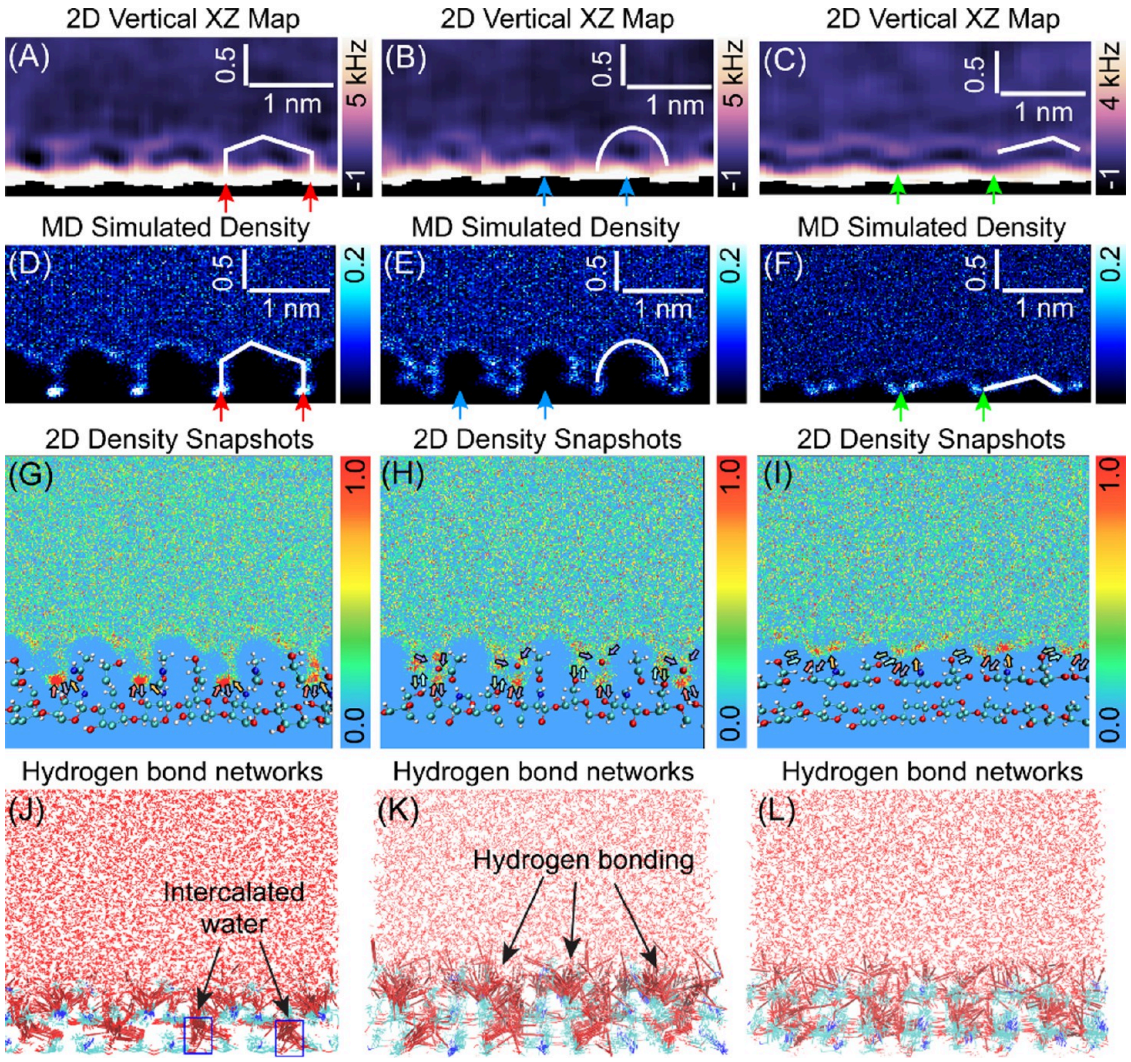

Figure 9. Comparison between water-oxygen density maps and experimentally obtained vertical Δf maps. (A−C) Vertical 2D-*xz* Δf maps taken along the dashed lines labeled (1) and (4) in Figure 6F and (6) in Figure 7C, respectively. (D−F) Vertical 2D water-oxygen density maps along the chain direction at different lateral positions on the (1−20) crystalline plane of the β-chitin NC. The red, blue, and green arrows indicate the identical hydration features between the simulation and experiment. (G−I) Water-oxygen density snapshots (40) with overlaid chitin molecular structures. (J−L) Hydrogen-bonding networks formed between water molecules and the underlying chitin substrate.

To further understand the water structure on β-chitin NCs, we compared simulated 2D XY water density slices (Figure 8D−I) and the horizontal in-plane 2D Δf XY maps acquired by 3D-AFM experiments (Figure 8Q). Notably, the comparison between Δf maps and MD water density distributions has been validated on other heterogeneous surfaces.[56,57] For small-amplitude oscillations, changes in Δf are directly proportional to the force gradient, confirming that both Δf and force maps exhibit identical hydration features. The in-plane water-density distribution and molecular organization across the hydration layers are evaluated using simulated 2D density slices above the (1−20) crystal plane, passing through z = 1.35−0.3 nm within the hydration layers. Initially, a circular dark depression, surrounded by a high-density region (Figure 8D; highlighted by white circles) at z = 1.35 nm, undergoes a structural transformation, evolving into extended hydration features that bridge two high-density water regions at z = 1.23 nm (Figure 8E; white rectangles). Subsequently, these distinctive hydration structures develop into protruding features with a dimer or dot-like shape, oriented at an angle of 49° to the chain axis (highlighted by green rectangles). The high-density molecular features along the b'-axis, perpendicular to the chain molecular axis, have a periodicity of approximately 1.38 nm (Figure 8F), which is consistent with the experiment (Figures 2D, 3D, S4, and S5), reflecting the underlying chitin crystalline plane symmetry. These characteristics of the changes in the water density arrangements are consistent with the experimentally observed water structures (Figure 8Q). Based on the 2D XY Δf slices extracted from larger (0.76 nm) to closer (0.30 nm) distances, the hydration structures exhibit identical changes. Notably, a diagonally staggered arrangement of the hydration features is evident at the interface (z = 0.30 nm), providing further validation for the simulation. The presence of distinct hydration structures at both short (0.3−0.35 nm) and intermediate (0.4−0.55 nm) distances from the chitin surface, as well as the overall extension of the hydration layers up to 0.6−0.7 nm, further confirmed by the radial distribution functions (RDFs) between water oxygens atoms and chitin oxygen/nitrogen surface atoms (Figure S21).

The 2D vertical Δf patterns frequently observed in our experiments (Figures 9A−C) were compared with simulated interfacial water-oxygen density distribution maps at three

https://doi.org/10.1021/jacs.5c08484
J. Am. Chem. Soc. 2025, 147, 39134−39150

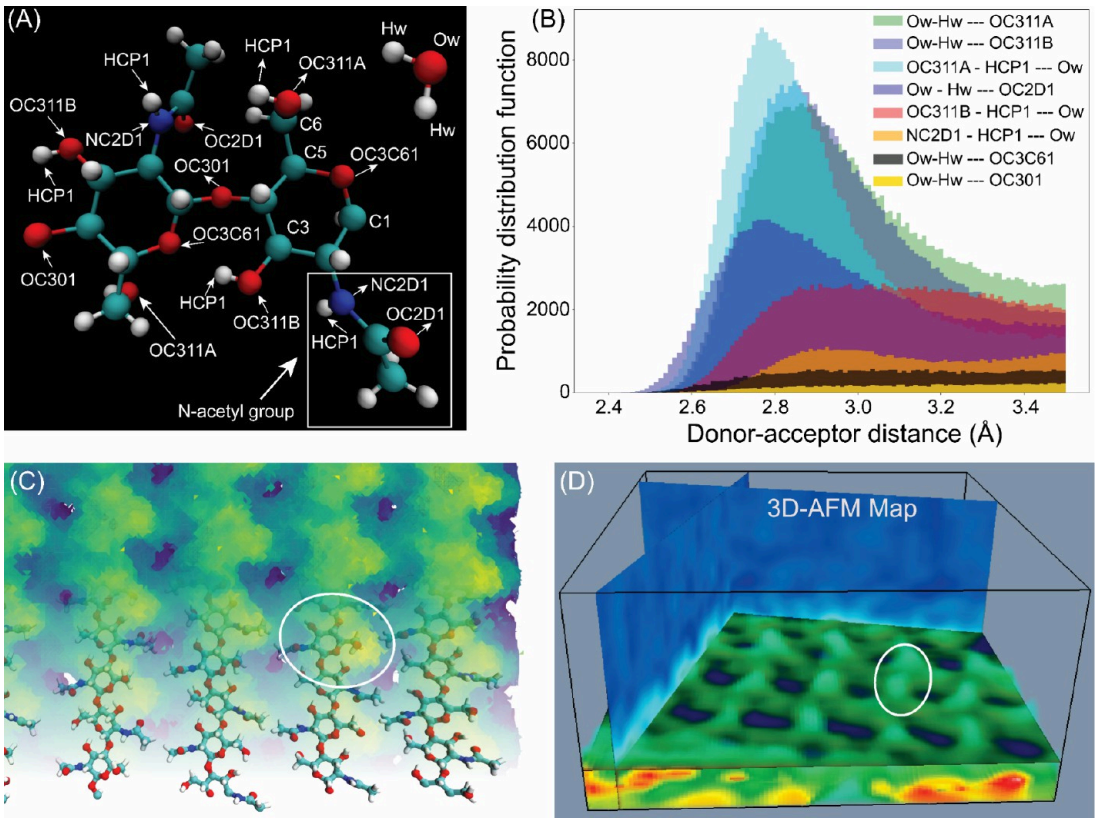

Figure 10. Hydrogen bonding analysis. (A) Atomic structures of the chitin chain and water with the corresponding labels used in the hydrogen bond analysis. Chitin and water molecules are displayed in a ball-and-stick model. Carbon atoms are represented in cyan, nitrogen atoms in blue, oxygen atoms in red, and hydrogen atoms in gray. (B) Hydrogen bond analysis between possible chitin sites and water molecules, showing the distribution of the number of hydrogen bonds formed between water and chitin chains. (C) Water-oxygen density snapshots, with the underlying structure of the (1−20) crystalline plane overlaid, reveal that water is mainly localized over the OH groups. (D) 3D-AFM map of the β-chitin NC−water interface visualized by Voxler software, showing apparent 2D slices in the horizontal (XY) and vertical (XZ) planes.

lateral positions to provide a rationale for vertical water organization. The water density distribution predicted by the MD simulation reproduces well the experimentally observed hydration structures (Figure 9D−F). The 2D vertical-hydration patterns shown in Figure 9A−C demonstrate that water molecules can interconnect with the surface below them through direct hydrogen bonding, referred to as "bound water." This phenomenon, also described as the nonfreezing state of water due to conformational restrictions on water mobility,[58] is further discussed in the Supporting Information, where definitions of "bound water," "intercalated water," and "water hydration" are provided. The regions of high water density, indicated by red arrows in Figure 9A,D, demonstrate the presence of bound water at the interface. The darker areas below the zigzag hydration patterns in Figure 9A,C, as well as the darker regions with empty voids within the semicircular hydration pattern in Figure 9B, indicate relative water depletion compared with bulk water density. This depletion can be attributed to a combination of hydrophobic confinement and the hydrophilic attraction of water molecules in nearby regions.

The MD snapshots of the water-oxygen density distribution in Figure 9G−I and the corresponding hydrogen bonding networks in Figure 9J−L closely follow the contours of surface topology, resulting in a pattern similar to the experimentally observed 2D vertical hydration profile (Figure 9A−C). The water molecules approach the surface above the space between the chitin layers and/or between individual chains and form hydrogen bonds over the OH groups located on C6 and C3. Moreover, relatively less molecular interaction occurs over the topographically more exposed N-acetyl groups (Figure 9J−L). The specific arrangement of the surface OH groups confines the water molecules to a specific density profile. This observation was further supported by the hydrogen bond analysis between water and specific chitin sites (Figure 10). Water molecules were observed to interact significantly with chitin OH groups located at two specific sites: C6 (OC311A-HCP1) and C3 (OC311B-HCP1). By contrast, the interactions with the OH groups located within the N-acetyl groups (OC2D1) were less pronounced. The RDFs between water-oxygen atoms and these specific chitin sites further substantiate these findings (Figures S21 and S22). The hydrogen bond analysis, combined with the MD hydrogen bond snapshots with overlaid underlying surface features, indicates that high water density is mainly confined in the OH regions (Figure 10A,B). A notable similarity is observed between the water-oxygen density snapshot and the 2D xy Δf section extracted from the 3D-AFM map of the β-chitin NC−water interface (Figure 10C,D).

DISCUSSION

The detailed molecular and hierarchical structures of β-chitin NCs revealed in our study have important implications for both their biological roles and materials performance. The complex organization of chitin chains and their associated hydration layers govern critical physicochemical properties,

https://doi.org/10.1021/jacs.5c08484
J. Am. Chem. Soc. 2025, 147, 39134−39150

including susceptibility to enzymatic degradation, mechanical strength, and interfacial interactions. Water-mediated hydrogen bonding networks reinforce the high crystallinity of β-chitin NCs while regulating enzymatic accessibility and molecular binding events at their surfaces, thereby bearing significant implications for both chitin degradation pathways and the design of chitin-based functional nanomaterials.

At the molecular scale, β-chitin NCs exhibit intricate structural arrangements and corrugations. These unprecedented molecular arrangements display a high degree of crystallinity, which can be attributed to the improvement and reinforcement of interfacial hydrogen-bonding networks facilitated by the incorporation of water molecules (Figures 2−4), as well as the enhanced structural stability conferred by water-mediated hydration layers, resulting in the improved organization and alignment of individual chitin surface chains. To investigate potential structural changes in both the surface crystalline architecture and surrounding hydration layers, we also performed experiments under acidic conditions. Our results indicate that the high degree of crystallinity observed at neutral pH (Figures 2−4 and 6) is maintained even in low-pH acetic acid buffer solutions (pH 3−5), as shown in Figures S23−S26. Water plays an essential role in the production processes of chitin NCs, either through direct interactions or as a reagent. In particular, water acts as a reaction medium during the hydrolysis of chitin or other polysaccharide crystals, facilitating the free diffusion of enzymes and reactants, which interact with the disordered domains on the crystal surfaces.[58,59] Although previous NMR and diffraction techniques have captured certain aspects of chitin−water interactions,[7] our 3D-AFM measurements provide, for the first time, direct visualization of the 3D arrangement of water molecules at chitin−water interfaces with subnanometer resolution at the single-fiber level. Our AFM experiments and MD simulations demonstrated that the spatial arrangement of exposed surface functional groups—their distribution and accessibility for water interactions and hydrogen bonding—together with the local electrostatic forces arising from charged functional groups collectively govern the structuring of water near chitin surfaces.

A comparative analysis between β- and α-chitin NCs (Figures S27−S31) revealed polymorph-specific distinctions in hydration behavior. While both polymorphs exhibit similar molecular structuring near the (010) planes, the (1−20) surfaces of α-chitin display wider and deeper grooves, allowing greater water accumulation and the formation of more stable hydration layers. This was corroborated by AFM force measurements (Figure S28), which indicated higher hydration repulsion forces for α-chitin compared to β-chitin. Our findings suggest that the energetic penalty imposed by the hydration layers during molecular interactions with the chitin surface—such as host−guest binding—is more significant for α-chitin NCs. As a result, external ions and molecules must overcome higher energetic barriers to establish close contact with the chitin NC surfaces and interact with their surface functional groups. This higher energy barrier effectively reduces the accessibility of surface functional groups on α-chitin NCs, potentially limiting their reactivity in various biological/chemical processes. These differences may suggest variations in reactivity between α- and β-chitin NCs. The reduced hydration force and energy barrier facilitate interactions with other molecules or ions, making β-chitin more chemically reactive. These structural insights into surface and hydration architectures have important implications for both biological recognition and materials design. For instance, experimental studies have demonstrated that proteins derived from chitinases, responsible for the enzymatic breakdown of chitin, exclusively bind to either α-[60] or β-chitin.[61] MD simulations have further shown that the spatial organization and distribution of the structured water layers are critical factors in the polymorph-selective binding of peptides and proteins to chitin.[36] Our results, in this context, provide a mechanistic explanation for this polymorph-specific enzyme binding by revealing distinct water structuring at α- and β-chitin interfaces (Figures S27 and S28). The stronger hydration layers near α-chitin may reduce the accessibility of chitin binding sites, thereby affecting the chitinase binding affinity and catalytic efficiency. By comparison, the lower energetic penalty associated with the structured hydration environment of β-chitin may facilitate more rapid enzyme access and substrate turnover.

From a material perspective, understanding these hydration-mediated surface properties is essential for the rational design of chitin-based functional materials. For example, polysaccharide-based membranes have recently been used for bioprotonic devices to transport small molecules and ions into living organisms under controlled conditions.[62] Water hydration networks affect molecular/ionic diffusions, and understanding their molecular structures and properties will be useful for optimizing polysaccharide-based membrane transport properties for bioprotonic applications.[63] Additionally, such an understanding would facilitate the development of water-responsive hydrogel-based sensors using chitin fibers. The response behavior of the sensors can be tailored by the water content, offering promising applications in environmental monitoring.

In summary, the detailed molecular-level understanding enables precise control over the crystallinity and hydration layer architecture, which are essential for optimizing mechanical reinforcement, fiber dispersion, and interfacial compatibility in polymer nanocomposites. Moreover, these insights aid in the design of pH-responsive materials with tunable swelling and mechanical properties, as well as targeted surface functionalization and chemical modifications or grafting strategies to enhance polymer compatibility and enzymatic activity in biomass conversion. The complex 3D water structuring at chitin−water interfaces is particularly relevant for optimizing the deconstruction and processing strategies of chitin-based nanomaterials,[64] addressing the challenge of "hard-to-remove water" encountered in energy-intensive drying steps.[65] The observation of polymorph-specific hydration patterns further facilitates the development of biomaterials with selective molecular recognition, which is crucial for biosensing and drug delivery.

Collectively, this work links nanoscale interfacial structure to rational design strategies, advancing the effective development of sustainable, biobased nanomaterials for energy and biomedical applications.[66] Additionally, it provides valuable insights into the computational modeling of chitin surface interactions, crystallosolvate formation, and enzymatic hydrolysis, supporting the development of future material design strategies.

MATERIALS AND METHODS

Materials. The siboglinid tubeworm (*L. columna*) was collected from Sagami Bay (35°0.917'N, 139°13.4774'E, 999 m deep, Oct

https://doi.org/10.1021/jacs.5c08484
J. Am. Chem. Soc. 2025, 147, 39134−39150

2021) by a manipulator on the deep-submergence vehicle (DSV) *Shinkai 6500* during R/V *Yokosuka* cruise YK21−18C. The following steps were taken to prepare β-chitin NC suspensions, as described in ref 67. First, the tubes were cut into small pieces and soaked in a 2:1 mixture of $CHCl_3$ and CH_3OH for 1 day to extract lipids and lipoproteins. Subsequently, the tubes were washed with deionized water and treated with a 10% (2.5 M) NaOH solution under a nitrogen purge for 1 day. This NaOH treatment was repeated three times, and the tubes were washed with deionized water. To further purify the tubes, they were subjected to 0.3% $NaClO_2$ treatment for 1 h, four times, in an acetate buffer adjusted to pH 4.8 at 70 °C, followed by washing with deionized water. The purified tubes were acid hydrolyzed with 2 M HCl at a boiling temperature for 4 h under magnetic stirring, followed by washing with distilled water.

Preparation of Chitin Suspension for AFM Observations. An aqueous suspension of β-chitin NCs (with a concentration of 3.0 wt %) was initially diluted to a concentration of 0.005 wt % in Milli-Q water. The suspension was then sonicated using an ultrasonic homogenizer (MITSUI; 3 mm diameter tip, maximum power of 500 W). To avoid overheating during the sonication process, the chitin samples were placed in an ice bath and subject to four 5 min sonication cycles. For AFM analysis, chitin NC suspensions were prepared by placing a drop of the diluted specimen (120 μL, 0.005 wt %) onto a freshly cleaved mica substrate. After an incubation period of 30 min, the mica substrate was rinsed several times with 120 μL of Milli-Q water to further reduce the concentration of chitin NCs and remove unbound chitin NC entities. A brief sonication postprocess was performed before depositing the chitin NC suspension on the freshly prepared mica substrate to avoid the formation of chitin NC aggregates. The prepared chitin NCs had relatively positively charged surfaces at pH 6−7, as revealed by Zeta-potential measurements (38.5 mV), and exhibited strong binding to the negatively charged muscovite-mica substrate through electrostatic interactions. All sample preparations and experiments were conducted using Milli-Q deionized water with a resistivity of 18.2 M Omega cm.

FM-AFM Setup. The molecular-resolution surface and interface structural characterization of β-chitin NCs was performed with a homemade FM-AFM system operating in a liquid environment equipped with an ultralow-noise cantilever deflection sensor, featuring a deflection noise density of 7.8 fm/$\sqrt{\text{Hz}}$ at a laser power of 2 mW for NCH cantilevers at room temperature.[68] The AFM cantilever was oscillated by a highly stable photothermal-excitation system using an infrared laser beam with a wavelength of 785 nm. The homemade AFM scanning system was controlled by a commercial AFM controller (ARC2, Asylum Research, Oxford Instruments, USA). The tip−sample interaction force was detected as a frequency shift using a phase-locked loop (PLL) circuit, and the amplitude of the cantilever oscillation was kept constant using a PLL controller (OC4, SPECS, Germany). The AFM was operated in constant-frequency-shift (Δf) mode, where the tip−sample distance was adjusted to maintain constant Δf. Under typical molecular-resolution imaging conditions in liquid, the lateral spatial resolution of our instrument is approximately 0.1 nm, while the vertical (z) resolution can reach down to around 0.01 nm. We note that zero-scan maps in liquid showed AFM noise levels ranging from approximately 3.5 to 10 pm across measurement bandwidths of 50 to 100 Hz, which is typical for molecular-scale AFM imaging in liquid. The AFM images were acquired with cantilevers (160AC-NG, OPUS, Bulgaria) with a nominal spring constant of 26 N/m and a nominal tip radius <8 nm. We also used PPP-NCH-AuD cantilevers from NANOSENSORS (Switzerland), with a nominal spring constant of 42 N/m. We experimentally determined the individual spring constant of each cantilever using the standard thermal-tune method.[69] Scan rates and angles were optimized for improved resolution, and WSxM and Gwyddion software were used for AFM image rendering and data processing. The AFM topography images reported in this study were not subjected to any filtering but only to first-order image flattening and slope corrections using WSxM. Imagining the crystalline surface with small-amplitude cantilever oscillation is a challenging task for relatively large-diameter chitin NCs while avoiding cantilever scratching and displacement of chitin fiber on the surface. To overcome this, the back of the cantilever was coated with Al film using an ALD system to increase the oscillation amplitude, which ensures stable surface imaging without chitin-fiber displacement. In some cases, cantilevers were coated with Si (15 nm) by using a dc sputter coater (KST-CSPS-KFI) to enhance tip-apex stability and remove contaminants. High-resolution, molecularly resolved AFM images were acquired at multiple scan directions, both before and after force spectroscopy measurements, to verify the absence of any surface damage or contamination. We note that the measured properties of each cantilever used, along with the image acquisition parameters corresponding to each image, are provided in Table 1 of the Supporting Information.

Ξ-Potential Analysis. The ζ-potential of β-chitin NC (0.3 wt %) was measured at 25 °C using a particle analyzer (Delsa Nano HC, Beckman Coulter Inc., USA) based on electrophoretic light scattering.

XRD Analysis. The transmittance XRD measurements were performed to analyze the crystal structure of the β-chitin NCs in the dry and wet states. The β-chitin NC dispersion (0.3 wt %) was placed in a metallic folder with a quartz window. A part of the dispersion was freeze-dried and conditioned at 23 °C and 50% RH for 1 day before the measurement. The conditioned sample was placed in a metallic plate folder with a hole. The folders were positioned on a Rigaku NANOPIX SAXS system for transmittance XRD measurements. The measurement was employed using monochromatized and collimated CuKα radiation (λ = 0.1542 nm), operating at 40 kV and 30 mA, with a camera length of 63 mm and 2PHF beam stopper. The 2D pattern was recorded using a Rigaku HyPix-3000 hybrid detector. The recorded patterns were then converted to a 1D $2q$-intensity profile using Rigaku 2DP software.

FT-IR Spectra of β-Chitin. The β-chitin NC dispersion was freeze-dried, and the resulting solid was further dried at 105 °C for 1 h to remove residual water. The dehydrated sample was then exposed to D_2O vapor at 100% relative humidity at room temperature in a desiccator overnight, followed by drying under a vacuum at room temperature. FT-IR spectra of the samples before and after deuteration were recorded using the attenuated total reflectance (ATR) technique with an FT/IR-6100 spectrometer (JASCO, Japan). Spectra were collected with a resolution of 4 cm^{-1} and 128 scans. All spectra were normalized to the intensity of the absorption band at approximately 2900 cm^{-1} by using Spectra Manager software (JASCO, Japan).

3D-AFM Measurements. The 3D Δf maps of chitin−water interfaces were obtained using the 3D-AFM technique, developed by Fukuma et al.,[68] which involves both the vertical and lateral scanning of the tip to investigate the interaction forces between the tip and surface within the 3D interfacial space. A fast-sinusoidal signal was additionally applied to change the tip's z-position during the image acquisition and force mapping. While performing linear XY scans of the tip, Δf was recorded for each tip position, ensuring that the average value of the Δf set-point remained constant by regulating the averaged distance between the tip and sample by a z-feedback control with a weak integral gain. By continuously recording the force field acting on the tip for each position in the three spatial coordinates using small oscillation amplitudes of 1−2 Å, a 3D Δf volume map with high spatial resolution can be generated in real time, reflecting the spatial distribution of ions and structured water at the interface with a depth of several nanometers.

The cantilevers were photothermally driven at their resonance frequency with oscillation amplitudes ranging from 0.1 to 0.25 nm to determine the organization and distribution of local hydration layers. The frequency and amplitude range of the z-modulation signal during the 3D-AFM force mapping were 195.3 Hz and 3−4 nm, respectively. To map the interfacial hydration structures, a large-area scan of the surface was initially performed to locate individual chitin NCs that would be used to investigate the 3D hydration structures. Subsequently, localized surface imaging was conducted in smaller scan areas by using the standard 2D FM-AFM imaging mode to map the surface topography. Subsequently, the method was switched to 3D-AFM to map the local 3D hydration structure. Within a selected

https://doi.org/10.1021/jacs.5c08484
J. Am. Chem. Soc. 2025, 147, 39134−39150

surface area, a 3D-Δf map was obtained by recording the Δf in real-time with respect to the tip positions in 3D interfacial space on the chitin NC surface. The 3D-Δf map typically covered an area of 10−20 nm × 10−20 nm, divided into grids of 128 × 128 pixels, and was acquired by recording Δf in real-time with respect to the tip positions in 3D interfacial space on the chitin NC surface. The z data of the 3D map included 256 pixels. For the data analysis, the X- and Y-pixels were increased to 256 by linear interpolation. Our AFM system is housed in a temperature-controlled room and enclosed within an acoustic isolation hood. To ensure both mechanical and thermal stability of the instrument and sample stage, the system was powered on and allowed to thermally equilibrate for several hours prior to performing 3D-AFM measurements. Furthermore, drift correction algorithms were applied to the 2D XY Δf maps to mitigate distortion arising from thermal and mechanical drift. The instrumental drift rates of our AFM system were quantitatively assessed in both lateral directions through the analysis of sequential AFM images obtained during the high-resolution imaging of β-chitin nanocrystals in water. The measured drift rates were approximately 0.0075 nm/s along the x-axis and 0.0127 nm/s along the y-axis. These low drift rates confirm the system's high mechanical and thermal stability, ensuring data accuracy and reliability.

3D-AFM Data Processing. A custom-made data analysis software developed in LabVIEW (National Instruments, USA) was employed to process large-scale 3D force-mapping data and extract 2D sectional maps at various vertical and lateral positions. The following steps were taken to acquire the 3D force maps. Initially, baseline correction was applied to a region distant from the surface to ensure that force values at large tip−sample distances were aligned to a zero-force reference. The slope of the surface was adjusted by subtracting the average height from each line scan. The height correction was then performed. The resolution of the 3D Δf data was improved through linear interpolation, i.e., interpolation two times in the X and Y directions. Finally, the 3D Δf data were smoothed using a 3 × 3 averaging filter to reduce noise and enhance data clarity. Further details are available in ref 56.

Computational Details. A parallelogram-shaped β-chitin unit cell was assembled using the "chitin-builder" tool (https://github.com/soft-matter-theory-at-icmab-csic/chitin_builder), with four repetitions along the z-axis to avoid artificial interactions between periodic images. The β-chitin sheets were then enlarged by 0.2 nm in the b-axis direction, and 1000 water molecules were randomly positioned in the newly formed intrasheet corridors. This swollen β-chitin NC was then solvated with water in a box with dimensions 26.0 nm × 24.0 nm × 41.7 nm using Packmol.[70] The final system comprised 42,768 and 195,000 atoms for the β-chitin NCs and water molecules, respectively. Topology files for LAMMPS[71] were constructed using Moltemplate.[72] Water was modeled using the TIP3P model.[73] For chitin, we employed the CHARMM carbohydrate force field,[74] which has been demonstrated to be a robust and reliable choice for simulating chitin in aqueous environments.[75] This force field has been successfully applied to capture the temperature-dependent self-assembly of solvated chitin chains,[76] to quantify chitosan oligomer adhesion on α-chitin crystal surfaces in water,[77] and to describe hydration-controlled colloidal and interfacial behavior of chitin NCs.[78]

The system underwent a 3 ns equilibration phase (1 ns NVT, 1 ns NPT, and 1 ns NVT), followed by a 10 ns NVT production run. No exchange of water molecules was observed during these timeframes; the initially intercalated waters remained inside the NC and the external waters did not penetrate it. While it is plausible that water exchange events might occur in longer simulations, a thorough investigation of their frequency and dynamics would go beyond the scope of the current study as it would not measurably affect the resulting NCs hydration structures. A 1 fs time step was employed, and temperature control was achieved by using a Nosé−Hoover thermostat (T = 300 K, τ = 0.1 ps). For nonbonded interactions, a 9 Å cutoff was applied for Lennard−Jones interactions, and the particle−particle-particle-mesh method was used for electrostatics, with a 12 Å real-space cutoff and 10^{-6} accuracy. The simulations were performed on 512 cores (4 nodes with 128 MPI tasks per node), yielding a throughput of 5.45 ns/day. Hydrogen bonding analysis was performed using MDAnalysis,[79] defining bonds by a maximum water-oxygen to chitin−oxygen/nitrogen distance of 0.35 nm and a donor-hydrogen-acceptor angle of 100°. Water-oxygen density distributions were calculated by using MDAnalysis on a 0.1 Å grid, sampling 1000 frames at 10 ps intervals during the NVT production run.

■ ASSOCIATED CONTENT

Supporting Information

The Supporting Information is available free of charge at https://pubs.acs.org/doi/10.1021/jacs.5c08484.

Experiments; high-resolution structural comparisons of α-chitin and β-chitin NCs; FT-IR spectra of β-chitin; a comparison of hydration forces on α-chitin and β-chitin NCs; pH-dependent hydration structures and molecular organization of β-chitin NCs; high-resolution structure of α-chitin derived from *Phaeocystis globosa*; high-resolution AFM images of β-chitin NC structures in water and acetic buffer at pH 3.5 and 5. Additional data for 3D-AFM maps of β-chitin NC-water interfaces, MD simulations of β-chitin NC structure and water density distribution around β-chitin NCs (PDF)

■ AUTHOR INFORMATION

Corresponding Authors

Ayhan Yurtsever − *Nano Life Science Institute (WPI-NanoLSI), Kanazawa University, Kanazawa 920-1192, Japan*; orcid.org/0000-0003-3779-5196; Email: yurtsever@staff.kanazawa-u.ac.jp

Takeshi Fukuma − *Nano Life Science Institute (WPI-NanoLSI), Faculty of Frontier Engineering, and Division of Nano Life Science, Kanazawa University, Kanazawa 920-1192, Japan*; orcid.org/0000-0001-8971-6002; Email: fukuma@staff.kanazawa-u.ac.jp

Authors

Kazuho Daicho − *Institute of Engineering Innovation, School of Engineering, University of Tokyo, Tokyo 113-8656, Japan*

Fabio Priante − *Department of Applied Physics, Aalto University, Helsinki FI-00076, Finland*; orcid.org/0000-0001-7052-8570

Keisuke Miyazawa − *Nano Life Science Institute (WPI-NanoLSI) and Faculty of Frontier Engineering, Kanazawa University, Kanazawa 920-1192, Japan*; orcid.org/0000-0002-5012-8040

Mohammad Shahidul Alam − *Division of Nano Life Science, Kanazawa University, Kanazawa 920-1192, Japan*

Kazuki Miyata − *Nano Life Science Institute (WPI-NanoLSI), Faculty of Frontier Engineering, and Division of Nano Life Science, Kanazawa University, Kanazawa 920-1192, Japan*; orcid.org/0000-0002-1641-2160

Akinori Yabuki − *Research Institute for Global Change, Japan Agency for Marine-Earth Science and Technology (JAMSTEC), Yokosuka, Kanagawa 237-0061, Japan; Advanced Institute for Marine Ecosystem Change (WPI-AIMEC), Yokohama, Kanagawa 236-0001, Japan*

Noriyuki Isobe − *Research Institute for Marine Resources Utilization (MRU), Japan Agency for Marine-Earth Science and Technology (JAMSTEC), Yokosuka, Kanagawa 237-0061, Japan; Department of Biomaterials Sciences, Graduate School of Agricultural and Life Sciences, The University of Tokyo, Tokyo 113-8657, Japan*; orcid.org/0000-0001-8571-3373

Tsuguyuki Saito − *Department of Biomaterials Sciences, Graduate School of Agricultural and Life Sciences, The University of Tokyo, Tokyo 113-8657, Japan;* orcid.org/0000-0003-1073-6663

Adam S. Foster − *Nano Life Science Institute (WPI-NanoLSI), Kanazawa University, Kanazawa 920-1192, Japan; Department of Applied Physics, Aalto University, Helsinki FI-00076, Finland;* orcid.org/0000-0001-5371-5905

Complete contact information is available at: https://pubs.acs.org/10.1021/jacs.5c08484

Author Contributions

[¶]A.Y. and K.D. contributed equally to this work. The manuscript was written through contributions of all authors. All authors have given approval to the final version of the manuscript.

Notes

The authors declare no competing financial interest.

■ ACKNOWLEDGMENTS

This work was primarily supported by grants-in-aid for scientific research (21H05251, 20K05321, 22J01001, 22KJ1473, and 25K18274) from the Ministry of Education, Culture, Sports, Science, and Technology of Japan (MEXT), World Premier International Research Center Initiative (WPI), MEXT, Japan JST-CREST Program (JPMJCR22L3; JPMJCR24A4), the New Energy and Industrial Technology Development Organization (NEDO) program (JPNP18016 and PJ-ID 20001845), Japan JST-ASPIRE Program (JPMJAP2310), and JST-PRESTO Program (JPMJPR2508). The computing resources from the Aalto Science-IT project, CSC, and Helsinki are gratefully acknowledged. We thank the captain and crew of R/V *Yokosuka* for their great support of scientific activity during the expedition YK21-18C (PI: Dr. Hidetaka Nomaki). We extend thanks to the DSV *Shinkai 6500* team. We thank the NIES for providing us with the culture of *Phaeocystis globosa* NIES-1396.

■ REFERENCES

(1) Martin-Martinez, F. J.; Jin, K.; López Barreiro, D.; Buehler, M. J. The Rise of Hierarchical Nanostructured Materials from Renewable Sources: Learning from Nature. *ACS Nano* **2018**, *12* (8), 7425−7433.

(2) Zhu, Y.; Romain, C.; Williams, C. K. Sustainable polymers from renewable resources. *Nature* **2016**, *540* (7633), 354−362.

(3) Frka-Petesic, B.; Parton, T. G.; Honorato-Rios, C.; Narkevicius, A.; Ballu, K.; Shen, Q.; Lu, Z.; Ogawa, Y.; Haataja, J. S.; Droguet, B. E.; et al. Structural Color from Cellulose Nanocrystals or Chitin Nanocrystals: Self-Assembly, Optics, and Applications. *Chem. Rev.* **2023**, *123* (23), 12595−12756.

(4) Lee, S.; Hao, L. T.; Park, J.; Oh, D. X.; Hwang, D. S. Nanochitin and Nanochitosan: Chitin Nanostructure Engineering with Multiscale Properties for Biomedical and Environmental Applications. *Adv. Mater.* **2023**, *35* (4), No. 2203325.

(5) Montazerian, H.; Davoodi, E.; Baidya, A.; Badv, M.; Haghniaz, R.; Dalili, A.; Milani, A. S.; Hoorfar, M.; Annabi, N.; Khademhosseini, A.; et al. Bio-macromolecular design roadmap towards tough bioadhesives. *Chem. Soc. Rev.* **2022**, *51* (21), 9127−9173.

(6) Parhi, R. Drug delivery applications of chitin and chitosan: a review. *Environ. Chem. Lett.* **2020**, *18* (3), 577−594.

(7) Bai, L.; Liu, L.; Esquivel, M.; Tardy, B. L.; Huan, S.; Niu, X.; Liu, S.; Yang, G.; Fan, Y.; Rojas, O. J. Nanochitin: Chemistry, Structure, Assembly, and Applications. *Chem. Rev.* **2022**, *122* (13), 11604−11674.

(8) Kelly, J. A.; Giese, M.; Shopsowitz, K. E.; Hamad, W. Y.; MacLachlan, M. J. The Development of Chiral Nematic Mesoporous Materials. *Acc. Chem. Res.* **2014**, *47* (4), 1088−1096.

(9) Hou, J.; Aydemir, B. E.; Dumanli, A. G. Understanding the structural diversity of chitins as a versatile biomaterial. *Philos. Trans. R. Soc. A* **2021**, *379* (2206), 20200331.

(10) Narkevicius, A.; Parker, R. M.; Ferrer-Orri, J.; Parton, T. G.; Lu, Z.; van de Kerkhof, G. T.; Frka-Petesic, B.; Vignolini, S. Revealing the Structural Coloration of Self-Assembled Chitin Nanocrystal Films. *Adv. Mater.* **2022**, *34* (31), No. 2203300.

(11) Jin, J.; Lee, D.; Im, H.-G.; Han, Y. C.; Jeong, E. G.; Rolandi, M.; Choi, K. C.; Bae, B.-S. Chitin Nanofiber Transparent Paper for Flexible Green Electronics. *Adv. Mater.* **2016**, *28* (26), 5169−5175.

(12) Ifuku, S.; Saimoto, H. Chitin nanofibers: preparations, modifications, and applications. *Nanoscale* **2012**, *4* (11), 3308−3318.

(13) You, J.; Li, M.; Ding, B.; Wu, X.; Li, C. Crab Chitin-Based 2D Soft Nanomaterials for Fully Biobased Electric Devices. *Adv. Mater.* **2017**, *29* (19), No. 1606895.

(14) Naghdi, T.; Golmohammadi, H.; Yousefi, H.; Hosseinifard, M.; Kostiv, U.; Horák, D.; Merkoçi, A. Chitin Nanofiber Paper toward Optical (Bio)sensing Applications. *ACS Appl. Mater. Interfaces* **2020**, *12* (13), 15538−15552.

(15) Torres-Rendon, J. G.; Femmer, T.; De Laporte, L.; Tigges, T.; Rahimi, K.; Gremse, F.; Zafarnia, S.; Lederle, W.; Ifuku, S.; Wessling, M.; et al. Bioactive Gyroid Scaffolds Formed by Sacrificial Templating of Nanocellulose and Nanochitin Hydrogels as Instructive Platforms for Biomimetic Tissue Engineering. *Adv. Mater.* **2015**, *27* (19), 2989−2995.

(16) Sirajudheen, P.; Poovathumkuzhi, N. C.; Vigneshwaran, S.; Chelaveettil, B. M.; Meenakshi, S. Applications of chitin and chitosan based biomaterials for the adsorptive removal of textile dyes from water — A comprehensive review. *Carbohydr. Polym.* **2021**, *273*, No. 118604.

(17) Nasrollahzadeh, M.; Shafiei, N.; Nezafat, Z.; Soheili Bidgoli, N. S.; Soleimani, F. Recent progresses in the application of cellulose, starch, alginate, gum, pectin, chitin and chitosan based (nano)-catalysts in sustainable and selective oxidation reactions: A review. *Carbohydr. Polym.* **2020**, *241*, No. 116353.

(18) Deepthi, S.; Venkatesan, J.; Kim, S.-K.; Bumgardner, J. D.; Jayakumar, R. An overview of chitin or chitosan/nano ceramic composite scaffolds for bone tissue engineering. *Int. J. Biol. Macromol.* **2016**, *93*, 1338−1353.

(19) Mi, F.-L.; Shyu, S.-S.; Lin, Y.-M.; Wu, Y.-B.; Peng, C.-K.; Tsai, Y.-H. Chitin/PLGA blend microspheres as a biodegradable drug delivery system: a new delivery system for protein. *Biomaterials* **2003**, *24* (27), 5023−5036.

(20) Saralegi, A.; Fernandes, S. C. M.; Alonso-Varona, A.; Palomares, T.; Foster, E. J.; Weder, C.; Eceiza, A.; Corcuera, M. A. Shape-Memory Bionanocomposites Based on Chitin Nanocrystals and Thermoplastic Polyurethane with a Highly Crystalline Soft Segment. *Biomacromolecules* **2013**, *14* (12), 4475−4482.

(21) Kim, K.; Ha, M.; Choi, B.; Joo, S. H.; Kang, H. S.; Park, J. H.; Gu, B.; Park, C.; Park, C.; Kim, J.; et al. Biodegradable, electro-active chitin nanofiber films for flexible piezoelectric transducers. *Nano Energy* **2018**, *48*, 275−283.

(22) Tan, Y.; Hoon, S.; Guerette, P. A.; Wei, W.; Ghadban, A.; Hao, C.; Miserez, A.; Waite, J. H. Infiltration of chitin by protein coacervates defines the squid beak mechanical gradient. *Nat. Chem. Biol.* **2015**, *11* (7), 488−495.

(23) Facchinatto, W. M.; dos Santos, D. M.; de Lacerda Bukzem, A.; Moraes, T. B.; Habitzreuter, F.; de Azevedo, E. R.; Colnago, L. A.; Campana-Filho, S. P. Insight into morphological, physicochemical and spectroscopic properties of β-chitin nanocrystalline structures. *Carbohydr. Polym.* **2021**, *273*, No. 118563.

(24) Ragni, R.; Cicco, S. R.; Vona, D.; Farinola, G. M. Multiple Routes to Smart Nanostructured Materials from Diatom Microalgae: A Chemical Perspective. *Adv. Mater.* **2018**, *30* (19), No. 1704289.

(25) Blackwell, J. Structure of β-chitin or parallel chain systems of poly-β-(1→4)-N-acetyl-D-glucosamine. *Biopolymers* **1969**, *7* (3), 281−298.
(26) Tanner, S. F.; Chanzy, H.; Vincendon, M.; Roux, J. C.; Gaill, F. High-resolution solid-state carbon-13 nuclear magnetic resonance study of chitin. *Macromolecules* **1990**, *23* (15), 3576−3583.
(27) Sikorski, P.; Hori, R.; Wada, M. Revisit of α-Chitin Crystal Structure Using High Resolution X-ray Diffraction Data. *Biomacromolecules* **2009**, *10* (5), 1100−1105.
(28) Nishiyama, Y.; Noishiki, Y.; Wada, M. X-ray Structure of Anhydrous β-Chitin at 1 Å Resolution. *Macromolecules* **2011**, *44* (4), 950−957.
(29) Sawada, D.; Nishiyama, Y.; Langan, P.; Forsyth, V. T.; Kimura, S.; Wada, M. Direct Determination of the Hydrogen Bonding Arrangement in Anhydrous β-Chitin by Neutron Fiber Diffraction. *Biomacromolecules* **2012**, *13* (1), 288−291.
(30) Vincent, J. F. V.; Wegst, U. G. K. Design and mechanical properties of insect cuticle. *Arthropod Struct. Dev.* **2004**, *33* (3), 187−199.
(31) Yoshifuji, A.; Noishiki, Y.; Wada, M.; Heux, L.; Kuga, S. Esterification of β-Chitin via Intercalation by Carboxylic Anhydrides. *Biomacromolecules* **2006**, *7* (10), 2878−2881.
(32) Yurtsever, A.; Wang, P.-X.; Priante, F.; Morais Jaques, Y.; Miyata, K.; MacLachlan, M. J.; Foster, A. S.; Fukuma, T. Probing the Structural Details of Chitin Nanocrystal−Water Interfaces by Three-Dimensional Atomic Force Microscopy. *Small Methods* **2022**, *6* (9), No. 2200320.
(33) Saito, Y.; Okano, T.; Gaill, F.; Chanzy, H.; Putaux, J.-L. Structural data on the intra-crystalline swelling of β-chitin. *Int. J. Biol. Macromol.* **2000**, *28* (1), 81−88.
(34) Noishiki, Y.; Kuga, S.; Wada, M.; Hori, K.; Nishiyama, Y. Guest Selectivity in Complexation of β-Chitin. *Macromolecules* **2004**, *37* (18), 6839−6842.
(35) Sawada, D.; Kimura, S.; Nishiyama, Y.; Langan, P.; Wada, M. The crystal structure of mono-ethylenediamine β-chitin from synchrotron X-ray fiber diffraction. *Carbohydr. Polym.* **2013**, *92* (2), 1737−1742.
(36) Brown, A. H.; Walsh, T. R. Elucidating Polymorph-Selective Bioadsorption on Chitin Surfaces. *ACS Biomater. Sci. Eng.* **2019**, *5* (2), 594−602.
(37) Krajewska, B. Application of chitin- and chitosan-based materials for enzyme immobilizations: a review. *Enzyme Microb. Technol.* **2004**, *35* (2), 126−139.
(38) Petridis, L.; Smith, J. C. Molecular-level driving forces in lignocellulosic biomass deconstruction for bioenergy. *Nat. Rev. Chem.* **2018**, *2* (11), 382−389.
(39) Noishiki, Y.; Nishiyama, Y.; Wada, M.; Okada, S.; Kuga, S. Inclusion Complex of β-Chitin and Aliphatic Amines. *Biomacromolecules* **2003**, *4* (4), 944−949.
(40) Ifuku, S.; Kaminaka, H.; Shams, M. I. Nanochitin From Crab Shells: Production, Chemical Modification, Composite Materials, and Physiological Functions. *Macromol. Rapid Commun.* **2025**, *46* (9), 2400765.
(41) Sawada, D.; Nishiyama, Y.; Langan, P.; Forsyth, V. T.; Kimura, S.; Wada, M. Water in Crystalline Fibers of Dihydrate β-Chitin Results in Unexpected Absence of Intramolecular Hydrogen Bonding. *PLoS One* **2012**, *7* (6), No. e39376.
(42) Ogawa, Y.; Kimura, S.; Wada, M. Electron diffraction and high-resolution imaging on highly-crystalline β-chitin microfibril. *J. Struct. Biol.* **2011**, *176* (1), 83−90.
(43) Giessibl, F. J. Advances in atomic force microscopy. *Rev. Mod. Phys.* **2003**, *75* (3), 949−983.
(44) Fukuma, T.; Garcia, R. Atomic- and Molecular-Resolution Mapping of Solid−Liquid Interfaces by 3D Atomic Force Microscopy. *ACS Nano* **2018**, *12* (12), 11785−11797.
(45) Umeda, K.; Zivanovic, L.; Kobayashi, K.; Ritala, J.; Kominami, H.; Spijker, P.; Foster, A. S.; Yamada, H. Atomic-resolution three-dimensional hydration structures on a heterogeneously charged surface. *Nat. Commun.* **2017**, *8* (1), 2111.
(46) Nakouzi, E.; Stack, A. G.; Kerisit, S.; Legg, B. A.; Mundy, C. J.; Schenter, G. K.; Chun, J.; De Yoreo, J. J. Moving beyond the Solvent-Tip Approximation to Determine Site-Specific Variations of Interfacial Water Structure through 3D Force Microscopy. *J. Phys. Chem. C* **2021**, *125* (2), 1282−1291.
(47) Uhlig, M. R.; Martin-Jimenez, D.; Garcia, R. Atomic-scale mapping of hydrophobic layers on graphene and few-layer MoS2 and WSe2 in water. *Nat. Commun.* **2019**, *10* (1), 2606.
(48) Schlesinger, I.; Sivan, U. Three-Dimensional Characterization of Layers of Condensed Gas Molecules Forming Universally on Hydrophobic Surfaces. *J. Am. Chem. Soc.* **2018**, *140* (33), 10473−10481.
(49) Nakouzi, E.; Kerisit, S.; Legg, B. A.; Yadav, S.; Li, D.; Stack, A. G.; Mundy, C. J.; Chun, J.; Schenter, G. K.; De Yoreo, J. J. Solution Structure and Hydration Forces between Mica and Hydrophilic Versus Hydrophobic Surfaces. *J. Phys. Chem. C* **2023**, *127* (5), 2741−2752.
(50) Söngen, H.; Marutschke, C.; Spijker, P.; Holmgren, E.; Hermes, I.; Bechstein, R.; Klassen, S.; Tracey, J.; Foster, A. S.; Kühnle, A. Chemical Identification at the Solid−Liquid Interface. *Langmuir* **2017**, *33* (1), 125−129.
(51) Söngen, H.; Reischl, B.; Miyata, K.; Bechstein, R.; Raiteri, P.; Rohl, A. L.; Gale, J. D.; Fukuma, T.; Kühnle, A. Resolving Point Defects in the Hydration Structure of Calcite (10.4) with Three-Dimensional Atomic Force Microscopy. *Phys. Rev. Lett.* **2018**, *120* (11), No. 116101.
(52) Garcia, R. Interfacial Liquid Water on Graphite, Graphene, and 2D Materials. *ACS Nano* **2023**, *17* (1), 51−69.
(53) Miyata, K.; Adachi, K.; Miyashita, N.; Miyazawa, K.; Foster, A. S.; Fukuma, T. High-Speed Three-Dimensional Scanning Force Microscopy Visualization of Subnanoscale Hydration Structures on Dissolving Calcite Step Edges. *Nano Lett.* **2024**, *24* (35), 10842−10849.
(54) Martin-Jimenez, D.; Chacon, E.; Tarazona, P.; Garcia, R. Atomically resolved three-dimensional structures of electrolyte aqueous solutions near a solid surface. *Nat. Commun.* **2016**, *7* (1), 12164.
(55) Fukuma, T.; Higgins, M. J.; Jarvis, S. P. Direct Imaging of Lipid-Ion Network Formation under Physiological Conditions by Frequency Modulation Atomic Force Microscopy. *Phys. Rev. Lett.* **2007**, *98* (10), No. 106101.
(56) Yurtsever, A.; Wang, P.-X.; Priante, F.; Morais Jaques, Y.; Miyazawa, K.; MacLachlan, M. J.; Foster, A. S.; Fukuma, T. Molecular insights on the crystalline cellulose-water interfaces via three-dimensional atomic force microscopy. *Sci. Adv.* **2022**, *8* (41), No. eabq0160.
(57) Spijker, P.; Hiasa, T.; Musso, T.; Nishioka, R.; Onishi, H.; Foster, A. S. Understanding the Interface of Liquids with an Organic Crystal Surface from Atomistic Simulations and AFM Experiments. *J. Phys. Chem. C* **2014**, *118* (4), 2058−2066.
(58) Ajdary, R.; Tardy, B. L.; Mattos, B. D.; Bai, L.; Rojas, O. J. Plant Nanomaterials and Inspiration from Nature: Water Interactions and Hierarchically Structured Hydrogels. *Adv. Mater.* **2021**, *33* (28), No. 2001085.
(59) Österberg, M.; Henn, K. A.; Farooq, M.; Valle-Delgado, J. J. Biobased Nanomaterials—The Role of Interfacial Interactions for Advanced Materials. *Chem. Rev.* **2023**, *123* (5), 2200−2241.
(60) Zeltins, A.; Schrempp, H. Specific Interaction of the Streptomyces Chitin-Binding Protein Chb1 with α-Chitin. *Eur. J. Biochem.* **1997**, *246* (2), 557−564.
(61) Vaaje-Kolstad, G.; Houston, D. R.; Riemen, A. H. K.; Eijsink, V. G. H.; van Aalten, D. M. F. Crystal Structure and Binding Properties of the Serratia marcescens Chitin-binding Protein CBP21*. *J. Biol. Chem.* **2005**, *280* (12), 11313−11319.
(62) Bazargan, G.; Fischer, S. A.; Gunlycke, D. Effect of Structure and Hydration Level on Water Diffusion in Chitosan Membranes. *Macromol. Theory Simul.* **2021**, *30* (4), No. 2000064.

(63) Zhong, C.; Deng, Y.; Roudsari, A. F.; Kapetanovic, A.; Anantram, M. P.; Rolandi, M. A polysaccharide bioprotonic field-effect transistor. *Nat. Commun.* **2011**, *2* (1), 476.
(64) Tardy, B. L.; Mattos, B. D.; Otoni, C. G.; Beaumont, M.; Majoinen, J.; Kämäräinen, T.; Rojas, O. J. Deconstruction and Reassembly of Renewable Polymers and Biocolloids into Next Generation Structured Materials. *Chem. Rev.* **2021**, *121* (22), 14088−14188.
(65) Salem, K. S.; Barrios, N.; Jameel, H.; Pal, L.; Lucia, L. Computational and experimental insights into the molecular architecture of water-cellulose networks. *Matter* **2023**, *6* (5), 1366−1381.
(66) Ling, S.; Kaplan, D. L.; Buehler, M. J. Nanofibrils in nature and materials engineering. *Nat. Rev. Mater.* **2018**, *3* (4), 18016.
(67) Kaku, Y.; Fujisawa, S.; Saito, T.; Isogai, A. Synthesis of Chitin Nanofiber-Coated Polymer Microparticles via Pickering Emulsion. *Biomacromolecules* **2020**, *21* (5), 1886−1891.
(68) Fukuma, T. Wideband low-noise optical beam deflection sensor with photothermal excitation for liquid-environment atomic force microscopy. *Rev. Sci. Instrum.* **2009**, *80* (2), No. 023707.
(69) Hutter, J. L.; Bechhoefer, J. Calibration of atomic-force microscope tips. *Rev. Sci. Instrum.* **1993**, *64* (7), 1868−1873.
(70) Martínez, L.; Andrade, R.; Birgin, E. G.; Martínez, J. M. PACKMOL: A package for building initial configurations for molecular dynamics simulations. *J. Comput. Chem.* **2009**, *30* (13), 2157−2164.
(71) Thompson, A. P.; Aktulga, H. M.; Berger, R.; Bolintineanu, D. S.; Brown, W. M.; Crozier, P. S.; in't Veld, P. J.; Kohlmeyer, A.; Moore, S. G.; Nguyen, T. D.; et al. LAMMPS - a flexible simulation tool for particle-based materials modeling at the atomic, meso, and continuum scales. *Comput. Phys. Commun.* **2022**, *271*, No. 108171.
(72) Jewett, A. I.; Stelter, D.; Lambert, J.; Saladi, S. M.; Roscioni, O. M.; Ricci, M.; Autin, L.; Maritan, M.; Bashusqeh, S. M.; Keyes, T.; et al. Moltemplate: A Tool for Coarse-Grained Modeling of Complex Biological Matter and Soft Condensed Matter Physics. *J. Mol. Biol.* **2021**, *433* (11), No. 166841.
(73) Jorgensen, W. L.; Chandrasekhar, J.; Madura, J. D.; Impey, R. W.; Klein, M. L. Comparison of simple potential functions for simulating liquid water. *J. Chem. Phys.* **1983**, *79* (2), 926−935.
(74) Guvench, O.; Mallajosyula, S. S.; Raman, E. P.; Hatcher, E.; Vanommeslaeghe, K.; Foster, T. J.; Jamison, F. W., II; MacKerell, A. D., Jr CHARMM Additive All-Atom Force Field for Carbohydrate Derivatives and Its Utility in Polysaccharide and Carbohydrate−Protein Modeling. *J. Chem. Theory Comput.* **2011**, *7* (10), 3162−3180.
(75) Wei, A.; Fu, J.; Guo, F. Mechanical properties of chitin polymorphs: A computational study. *J. Mater. Sci.* **2021**, *56* (20), 12048−12058.
(76) Romany, A.; Payne, G. F.; Shen, J. Mechanism of the Temperature-Dependent Self-Assembly and Polymorphism of Chitin. *Chem. Mater.* **2023**, *35* (16), 6472−6481.
(77) Hudek, M.; Kubiak-Ossowska, K.; Johnston, K.; Ferro, V. A.; Mulheran, P. A. Chitin and Chitosan Binding to the α-Chitin Crystal: A Molecular Dynamics Study. *ACS Omega* **2023**, *8* (3), 3470−3477.
(78) Su, X.; Wan, Z.; Lu, Y.; Rojas, O. Control of the Colloidal and Adsorption Behaviors of Chitin Nanocrystals and an Oppositely Charged Surfactant at Solid, Liquid, and Gas Interfaces. *Langmuir* **2024**, *40* (9), 4881−4892.
(79) Michaud-Agrawal, N.; Denning, E. J.; Woolf, T. B.; Beckstein, O. MDAnalysis: A toolkit for the analysis of molecular dynamics simulations. *J. Comput. Chem.* **2011**, *32* (10), 2319−2327.

https://doi.org/10.1021/jacs.5c08484
J. Am. Chem. Soc. 2025, 147, 39134−39150